Coupled analysis of seawater and sedimentary $^{231}Pa/^{230}Th$ in the tropical Atlantic.

Hong Chin Ng[a,*], Laura F. Robinson[a], George H. Rowland[a], Siyuan Sean Chen[a,b,1], Jerry F. McManus[c]

[a] School of Earth Sciences, University of Bristol, Bristol

[b] Department of Geology and Geophysics, Woods Hole Oceanographic Institution, Woods Hole, MA, USA

[c] Department of Earth and Environmental Sciences, Columbia University and the Lamont-Doherty Earth Observatory of Columbia University, Palisades, NY 10964, USA

*email: hn9381@bristol.ac.uk

Keywords: Protactinium, Thorium, Sediment-seawater analysis, Scavenging, Eddy diffusion, Advection, Hydrothermal scavenging, Transient nepheloid layer, Boundary scavenging, Tropical Atlantic

[1] Now at MIT-WHOI Joint Program in Oceanography, Massachusetts Institute of Technology, Cambridge, MA, USA

Abstract

The $^{231}Pa/^{230}Th$ ratio of seawater and in ocean sediments is a potentially powerful tool in tracing oceanic processes such as the ocean circulation and marine primary productivity. However, $^{231}Pa/^{230}Th$ reflects the combined signal of multiple controls associated with scavenging and oceanic transport, limiting its use as a paleo-proxy. Given that links between seawater and sedimentary ^{231}Pa and ^{230}Th distributions are crucial for understanding the cycling and removal fluxes of these nuclides, we carry out analysis of ^{231}Pa and ^{230}Th in both seawater (dissolved phase) and modern sediment samples acquired from five depth transects across the northern tropical Atlantic open ocean. Overall, the sediment data support the dominance of ^{231}Pa export in the deep Atlantic Ocean (>2.5 km) associated with the southward advection of North Atlantic Deep Water. However, the seawater data provide evidence for locally enhanced scavenging of ^{231}Pa and ^{230}Th near the western seamounts that is likely to be associated with the influence of hydrothermal activity or episodic formation of transient nepheloid layers. At shallower depths (0.5–1.5 km), paired sediment and seawater $^{231}Pa/^{230}Th$ data reveal enhanced burial of ^{231}Pa at the eastern and mid-Atlantic sites that is likely related to elevated marine primary productivity and/or influence of boundary scavenging at the African margin, and a net input of ^{231}Pa potentially maintained by the northward advection of intermediate water masses and an additional mechanism of upward diffusion. Our findings provide greater insights into the range of oceanic processes that play a significant role in the cycling of ^{231}Pa and ^{230}Th, with implications for the controls of $^{231}Pa/^{230}Th$ distribution in the Atlantic Ocean.

1. INTRODUCTION

Research studies since the late twentieth century have established the potential in utilizing two U-series radionuclide isotopes, ^{231}Pa and ^{230}Th to trace oceanic processes based on the fractionation between the two isotopes due to the difference in particle reactivity (Henderson and Anderson, 2003). Observations indicate that such fractionation can occur due to spatial variations in the removal rates of the isotopes from seawater by scavenging (dominantly by adsorption of the isotopes onto sinking particulate matter) (Anderson et al., 1983a, b; Yang et al., 1986), and due to horizontal transport by water mass advection (Yu et al., 1996) and diffusion down a concentration gradient (Bacon, 1988). Following this concept, subsequent works have produced paleo-proxy applications of sedimentary $^{231}Pa_{ex,0}/^{230}Th_{ex,0}$, which is defined as the activity ratio of ^{231}Pa and ^{230}Th unsupported by the decay of parent U radionuclides in the sediment and corrected for post-depositional decay (Henderson and Anderson, 2003) (hereafter $^{231}Pa/^{230}Th$). Sedimentary

$^{231}Pa/^{230}Th$ has been used as a proxy of opal-dominant marine primary productivity in the Southern Ocean (Anderson et al., 2009; Bradtmiller et al., 2009; Kumar et al., 1993) and the equatorial Pacific (Bradtmiller et al., 2006; Costa et al., 2017; Pichat et al., 2004; Thiagarajan and McManus, 2019), and as a proxy of Atlantic Meridional Overturning Circulation (AMOC) strength in the Atlantic (Henry et al., 2016; Hoffmann et al., 2018; Lippold et al., 2011; McManus et al., 2004; Ng et al., 2018). Both applications are useful for constraining the forcing-feedback relationships between the climate and ocean. This is because Southern Ocean productivity plays a critical role in the global biological pump which regulates the major greenhouse gas atmospheric carbon dioxide (Sigman et al., 2010); while the AMOC is a key player in meridional heat transport (Johns et al., 2011). The use of sedimentary $^{231}Pa/^{230}Th$ as a paleo-proxy, however, is still restricted as it reflects mixed signals of multiple controls that are not straightforward to deconvolve (Missiaen et al., 2019; Rempfer et al., 2017; Siddall et al., 2005). Indeed, the proxy applications above are mainly constrained to specific regions where one control appears to be dominant. To overcome this limitation, seawater (Deng et al., 2018; Grenier et al., 2019; Hayes et al., 2015a; Hayes et al., 2013; Pavia et al., 2018) and sediment (Bradtmiller et al., 2014; Costa et al., 2017; Hoffmann et al., 2013; Lippold et al., 2012) analyses and modelling studies (Gu and Liu, 2017; Lerner et al., 2020; Missiaen et al., 2019; Missiaen et al., 2020; Rempfer et al., 2017) are now revealing a detailed and quantitative picture of the processes that govern the cycling of ^{231}Pa and ^{230}Th in the ocean.

The ^{231}Pa and ^{230}Th isotopes dissolved in seawater originate principally from the radioactive decay of dissolved ^{235}U and ^{234}U isotopes respectively. The production rates of ^{231}Pa and ^{230}Th in the ocean are relatively constant due to the largely uniform salinity-normalized U concentration dissolved in seawater (Owens et al., 2011), with the derived production ratio of $^{231}Pa/^{230}Th$ being ~0.093 (Anderson et al., 1983b). The two isotopes are rapidly scavenged by sinking particulates, and their ocean residence times estimated from seawater dissolved concentrations are 10–40 years for ^{230}Th and 50–200 years for ^{231}Pa (Henderson and Anderson, 2003). Based on their seawater concentration profiles, ^{231}Pa and ^{230}Th are thought to undergo reversible scavenging, which is the continuous exchange of the particle-reactive isotopes between the dissolved phase and the particulate surface-bound phase through adsorption and desorption prior to deposition on seafloor sediments (Bacon and Anderson, 1982; Lerner et al., 2016; Nozaki et al., 1987).

The ongoing coordinated international effort of GEOTRACES (Frank et al., 2003) has provided valuable datasets that aid evaluation of the scavenging and advection controls of $^{231}Pa/^{230}Th$ (Deng

et al., 2014; Grenier et al., 2019; Hayes et al., 2015a; Hayes et al., 2013; Pavia et al., 2018). The Atlantic Ocean has been one of the most studied regions, due to the wide interest in the quantitative link between $^{231}Pa/^{230}Th$ and AMOC transport, particularly the advection of North Atlantic Deep Water (NADW). Seawater (Deng et al., 2018; Deng et al., 2014), sediment observations (Bradtmiller et al., 2014; Lippold et al., 2012; McManus et al., 2004; Ng et al., 2018; Yu et al., 1996), and modelling studies (Missiaen et al., 2019; Missiaen et al., 2020; Rempfer et al., 2017; Siddall et al., 2005) all support an overall export of the more soluble ^{231}Pa relative to ^{230}Th out of the Atlantic basin driven by AMOC transport. The main sink of this exported ^{231}Pa appears to be associated with the elevated opal production south of the Antarctic polar front, as ^{231}Pa preferentially adsorbs onto opal particles (Moran et al., 2002). In addition, GEOTRACES studies (Deng et al., 2014; Hayes et al., 2015a) have highlighted the presence of notable sinks of ^{231}Pa and ^{230}Th in regions of intensified particle flux (or concentration), such as boundary scavenging at the African margin driven by elevated marine productivity and continental input, and bottom scavenging at the nepheloid layers where there are pronounced resuspension of seafloor sediments. Active hydrothermal vents at the Mid-Atlantic Ridge (MAR) have also been identified as evident sinks of the two isotopes, as both ^{231}Pa and ^{230}Th are efficiently scavenged by the elevated levels of Fe and Mn oxy-hydroxides in hydrothermal plumes (Hayes et al., 2015a; Hayes et al., 2015b). High particle abundance in hydrothermal plumes (Estapa et al., 2015) might further contribute to the enhanced removal of the radionuclides from seawater. However, the presence of these marginal, nepheloid and hydrothermal sinks has been suggested based mainly on seawater observations, and links to sedimentary ^{231}Pa and ^{230}Th distribution are crucial in examining their removal fluxes in these settings of apparently enhanced scavenging.

Here we present paired seawater and sediment core-top ^{231}Pa and ^{230}Th analyses from the northern tropical Atlantic, with locations in open ocean settings of both east and west basins and from the MAR (Figs. 1 & 2). The study sites are under the influence of distinct water masses propagating at different water depths, and are located both near and far from continental margins, potential nepheloid layers and hydrothermal systems (Figs. 1 & 2). We aim to utilise the coupled seawater-sediment analyses to provide an improved understanding of the mechanisms regulating the present-day ^{231}Pa and ^{230}Th distributions in the Atlantic Ocean.

2. SAMPLES AND SITES

2.1. Paired core-top sediment and seawater samples

Twenty sediment core-top and twenty seawater samples used here for ^{231}Pa and ^{230}Th analyses span a water depth range of 0.5–4.6 km and latitudinal range of 5–15^{o} N across the Atlantic Ocean (Rowland et al., 2017). The core-top and seawater samples consist of 5 depth transects here named after the relevant seamounts and Vema fracture zone, which include the Carter Seamount and the Knipovich Seamount located in the eastern basin of the Atlantic, the Mid-Atlantic seamounts sitting on a transverse ridge south of the Vema fracture zone, the Vayda Seamount and the Gramberg Seamount located west of the MAR (Figs. 1 & 2). The core-top sediments were dated with the ^{14}C method, and the derived ages were in the range of 1.0–8.8 thousand years before present (ka BP) (Rowland et al., 2017), indicating Holocene ages for the core-top sediments.

2.2 Oceanic settings of the study area

In the northern tropical Atlantic, the southward-propagating NADW, characterised by salinity of 34.9–35.0, occupies the 1.5–4 km depth range (Fig. 2a). The upper portion of the NADW (UNADW) has been distinguished from the lower portion (LNADW) by the silicate concentration minima (11–25 µmol/kg) observed in the 1.5–2.5 km depth range (Fig. 2b). The UNADW is mainly composed of modified Labrador Seawater, while the LNADW largely consists of modified Nordic overflow waters (Jenkins et al., 2015). Decreasing salinity (<34.8, Fig. 2a) and increasing silicate concentration (>50 µmol/kg, Fig. 2b) below 4 km depth indicate an increased influence of the Antarctic Bottom Water sourced from the Southern Ocean, and this bottom water mass is referred to here as the modified AABW (mAABW). Sample sites sitting at intermediate depths (0.5–1.5 km) are mainly bathed in a mix of northward-propagating Antarctic Intermediate Water (AAIW) and Upper Circumpolar Deep Water (UCDW) (Oudot et al., 1998). The mixture of intermediate water masses, characterised by low salinity (34.5–34.8, Fig. 2a) and elevated silicate concentration (22–35 µmol/kg, Fig. 2b), is known here as the modified AAIW (mAAIW).

Satellite observations of surface chlorophyll concentration (NASA Goddard Space Flight Center, 2018 Reprocessing) suggest that marine primary productivity above Carter, Knipovich and Vema (the eastern and mid-Atlantic sites) is generally higher than that above Vayda and Gramberg (the western sites) (Fig. 1). The Vema, Vayda and Gramberg sites are also situated relatively proximal to active hydrothermal vent fields previously observed (Beaulieu et al., 2013) along the MAR (Fig. 1). The study area is also in the vicinity of nepheloid layers that were previously found off the

North African margin, and to the north of Amazon outflow (north of Brazil) (Gardner et al., 2018a; Gardner et al., 2018b).

3. METHODS

3.1. Beam attenuation coefficient as a proxy of seawater particle concentration

A Chelsea/Seatech transmissometer (s/n: 09-7107-001) integrated with the CTD rosette was used to measure light transmissivity in seawater at the study sites. The transmissometer measurement was used to calculate the beam attenuation coefficient (m^{-1}) (Equation 1), which has been used as a proxy of particle concentration in seawater, and to identify nepheloid layers at depth (Gardner et al., 2018a; Hayes et al., 2015a).

Equation 1. Beam attenuation coefficient = $-(1/r) * \ln(Tr)$

where r is the beam path length of the transmissometer (0.25 m), and Tr is the fraction of beam transmission relative to the initial beam intensity.

3.2. Sediment Fe/Ti as tracer of hydrothermal activity

Using the ITRAX X-ray Fluorescence (XRF) core scanner in the British Ocean Sediment Core Research Facility, Fe and Ti data were generated for two sediment cores collected from Gramberg (JC094-GVY14: 15.464° N, 50.992° W, 2714 m depth) and Carter (JC094-GVY01: 7.435° N, 21.7963° W, 3426 m depth) (Ng et al., 2018) (Fig. 1). These two sediment cores had ^{14}C-based chronology established from a previous study (Ng et al., 2018). The main source for sediment/particulate Ti and Fe in the open ocean is atmospheric dust from the continent. Hydrothermal activity also provides significant amount of particulate Fe in a local scale, therefore surface sediments (Aquilina et al., 2014) and suspended particles in seawater (Ohnemus and Lam, 2015) from hydrothermal settings have been found to be enriched with Fe relative to Ti. Based on the principles above, sediment/particulate Fe/Ti ratio has been used as a tracer of hydrothermal activity (Aquilina et al., 2014; Ohnemus and Lam, 2015).

We defined an index of Fe/Ti, $I_{Fe/Ti}$, with lithogenic background as the standard reference (Equation 2). Following this definition, oceanic settings with Fe and Ti mainly derived from the continent would have $I_{Fe/Ti}$ of around 1, while those with additional supply of Fe from hydrothermal systems would have $I_{Fe/Ti}$ larger than 1. Here the sediment Fe/Ti from the Carter site located far from the MAR was used as the lithogenic background reference to derive $I_{Fe/Ti}$ for the sediments from the Gramberg site. As a comparison, $I_{Fe/Ti}$ was also calculated for other known

hydrothermal sites using previously published Fe/Ti data from these hydrothermal sites and lithogenic background Fe/Ti data from the surrounding region (Table 1).

Equation 2. $I_{Fe/Ti} = (Fe/Ti)_{\text{potential hydrothermal site of interest e.g. Gramberg}} / (Fe/Ti)_{\text{lithogenic background site, e.g. Carter}}$

3.3. Measurements of U-series isotopes

Analyses of seawater and sedimentary $^{231}Pa/^{230}Th$ were carried out by measuring U, Th and Pa isotopes with isotope dilution (Anderson and Fleer, 1982), employing the analytical protocols developed at the Bristol Isotope Group lab of University of Bristol (Ng et al., 2018; Rowland et al., 2017). Sample preparation first involved ^{236}U, ^{229}Th and ^{233}Pa spike addition to ~0.1 g powdered bulk sediments and 4–5 L seawater.

Sediment samples were then digested in a mix of concentrated HNO_3, HF and $HClO_4$ (7:3:2 volume ratio) on a hotplate set at 170^{o} C for >7 hours. Samples were evaporated to near dryness, and were further digested in concentrated HCl at 150^{o} C till the solutions became clear. Solutions were re-evaporated and re-dissolved in 2 M HCl.

Fe solution (97 mg) was added to the seawater samples. Actinide elements were co-precipitated with Fe hydroxide by adding ammonia solution (30 %) to both the digested sediment samples and the seawater samples until orange Fe precipitates started to form (pH 7–8). Given the large volume, seawater samples had to be set aside for 7 days, with intermittent shaking to ensure equilibration. Sediment and seawater samples were then centrifuged and supernatant liquids containing the bulk of major ions were discarded. The sample precipitates were washed three times by adding dilute ammonia (pH 7–8), centrifuging, and discarding supernatants, and the precipitates were then re-dissolved in concentrated HCl.

Chemical separation of U, Th and Pa was carried out with ion-exchange chromatography, using three sets of Environmental Express® polypropylene columns loaded with Eichrom Technologies® organic pre-filter resin 100–150 mesh followed by Eichrom 1-X8 anion exchange resin 100–200 mesh. The first set of columns involved separate elution of the Th fraction with concentrated HCl, elution of the Pa fraction with mixed HCl and trace HF, and elution of the U fraction with Milli-Q water. Th fraction was then purified using the second set of columns, where the Th fraction was loaded in HNO_3 (8 M), and was subsequently eluted with concentrated HCl. Pa fraction was

purified using the third set of columns, where the Pa fraction was loaded in concentrated HCl, and was subsequently eluted with mixed HCl and trace HF.

Analyses of the Th, Pa and U isotopes were then conducted with standard bracketing procedures using a Thermo-Finnigan Neptune, multi collector, inductively coupled plasma-mass spectrometer (MC-ICP-MS), and a CETAC Aridus desolvating nebuliser as the sample introduction system. The ^{229}Th and ^{230}Th isotopes were measured alternately on the Secondary Electron Multiplier (SEM), and the ^{231}Pa and ^{233}Pa isotopes were measured on a multi-ion counter (MIC) array to avoid dark noise building up on the SEM. Replicate analyses of a homogenised Southern Ocean siliceous ooze (Anderson et al., 2012) and an artificial seawater standard pre-calibrated at the Woods Hole Oceanographic Institution (Auro et al., 2012) were performed over the duration of this study, and the resulting ^{231}Pa and ^{230}Th measurements were generally in good agreement with reported calibrations (Table 2), demonstrating the reliability of our U-series analytical protocol.

Seawater and sedimentary $^{231}Pa_{ex}/^{230}Th_{ex}$ were calculated by correcting the ^{231}Pa and ^{230}Th measurements for fractions that are supported by the decay of lithogenic and authigenic U by assuming a lithogenic $^{238}U/^{232}Th$ activity ratio of 0.6 for the Atlantic Ocean. We found that the choice of lithogenic $^{238}U/^{232}Th$ within the uncertainty of the derived Atlantic average value (0.6 ± 0.1, or more recently, 0.55 ± 0.16) (Bourne et al., 2012; Henderson and Anderson, 2003) made no significant difference to the $^{231}Pa/^{230}Th$ values for our seawater and core-top sediment samples. The sedimentary ^{231}Pa and ^{230}Th measurements were also corrected for radioactive decay to the age of sediment deposition. Uncertainty in $^{231}Pa/^{230}Th$ measurements was propagated from internal errors associated with weighing, spike calibration and MC-ICP-MS measurements using a Monte-Carlo method.

3.4 Fractionation of ^{231}Pa and ^{230}Th, and sediment (flux) composition

The activity concentrations of ^{231}Pa and ^{230}Th were used to calculate their distribution coefficients, Kd_{Pa} and Kd_{Th} (Anderson et al., 1983a), defined as the ratios of the sediment (particulate) activity concentrations of the isotopes, $[^{231}Pa]_s$ and $[^{230}Th]_s$ (dpm/g), compared to the paired seawater dissolved activity concentrations, $[^{231}Pa]_d$ and $[^{230}Th]_d$ (dpm/g) (Equation 3). The relative fractionation of $^{231}Pa/^{230}Th$ between the seawater dissolved phase and the sediment particulate-adsorbed phase, $F_{Th/Pa}$ (Anderson et al., 1983a; Hayes et al., 2015b), was also calculated (Equation 4).

Equation 3. $Kd_{Th} = [^{230}Th]_s / [^{230}Th]_d$

$Kd_{Pa} = [^{231}Pa]_s / [^{231}Pa]_d$

Equation 4. $F_{Th/Pa} = Kd_{Th} / Kd_{Pa}$

Major composition of the core-top sediment samples: $CaCO_3$, biogenic opal, total organic carbon (TOC), and lithogenics have been reported in a previous study (Rowland et al., 2017) (Fig. 3a–d). Vertical sediment fluxes at the study sites were also estimated (Fig. 3e–i) using the ^{230}Th-normalisation method (Rowland et al., 2017). These data aid interpretation of Kd_{Pa}, Kd_{Th}, and $F_{Th/Pa}$, which have been suggested to reflect the affinity of the two isotopes to distinct chemical phases in the sinking particles/sediments (Chase et al., 2002; Geibert and Usbeck, 2004; Guo et al., 2002; Hayes et al., 2015b).

4. RESULTS

4.1. Beam attenuation coefficient

The highest beam attenuation coefficient values are observed in the top 50 m of the water column: 0.1–0.27 m^{-1}. Below that, beam attenuation coefficient falls rapidly to low levels (<0.05 m^{-1} below 500 m depth, <0.02 m^{-1} below 2500 m depth) at Knipovich, Vema and Vayda (Fig. 2c). In contrast, at the easternmost Carter depth transect, beam attenuation coefficient remains relatively elevated (~0.05 m^{-1} on average) from 200–4500 m (Fig. 2c).

4.2. Sediment Fe/Ti and $I_{Fe/Ti}$

Sediments from the Carter site have higher Fe and Ti content than those from the Gramberg site (Fig. 4a & b). Whilst there are large downcore changes in sediment Fe and Ti content for both Carter and Gramberg sediment cores (Fig. 4a & b), the Fe/Ti ratios of the two cores remain fairly constant downcore (Fig. 4c). The Gramberg sediment core overall has slightly higher Fe/Ti (~51 on average) than the core from Carter (~38 on average), and the Gramberg core records higher Fe/Ti variability between 5 and 20 cm depth (Fig. 4c).

The $I_{Fe/Ti}$ calculated for the Gramberg site (relative to the Carter site) (Equation 2) using the Fe/Ti data from the top 1 cm of the sediment cores (<4 ka, Fig. 4) is 1.29 ± 0.34. This value is lower than the $I_{Fe/Ti}$ calculated for other hydrothermal sites (Table 1). The $I_{Fe/Ti}$ for Hook Ridge (Aquilina et al., 2014), Rainbow hydrothermal field (Cave et al., 2002), Logatchev hydrothermal field (Chavagnac et al., 2008), and TAG hydrothermal field (Ohnemus and Lam, 2015) (relative to the lithogenic

background around these hydrothermal sites) are estimated to be 2.9 ± 0.1, 3.3 ± 1.5, 1.7 ± 0.4, and >3 respectively (Table 1).

4.3. Seawater and sedimentary $^{231}Pa/^{230}Th$

The ^{230}Th measurements of the seawater and core-top sediment samples have been reported in a previous study (Rowland et al., 2017). The measured tropical Atlantic seawater dissolved ^{231}Pa concentration ranges from 0.12–0.37 dpm/1000 kg. Similar to the ^{230}Th concentration (Rowland et al., 2017) (Fig. 5a), the ^{231}Pa concentration in seawater increases with depth from 0.5–1.5 km (Fig. 5b). However, below this depth range, the concentration and $^{231}Pa/^{230}Th$ profiles at Vayda display different trends compared to the eastern and mid-Atlantic sites (Carter, Knipovich and Vema). The eastern and mid-Atlantic sites show a coherent decrease in seawater dissolved $^{231}Pa/^{230}Th$ with increasing water depth below 1.5 km (Fig. 5c). This seawater $^{231}Pa/^{230}Th$ decrease is associated with (negative) deviations of dissolved ^{231}Pa and ^{230}Th concentration profiles from linear positive depth trends characteristic of reverse scavenging profiles (Bacon and Anderson, 1982), with greater deviations observed in the ^{231}Pa profiles (Fig. 5a & b). In contrast, Vayda exhibits considerably lower ^{230}Th and ^{231}Pa concentrations which persist at 0.1–0.2 dpm/1000 kg between 2 and 4 km water depth (Fig. 5a & b). The single seawater sample from Gramberg 2.7 km depth also shows low ^{230}Th and ^{231}Pa concentrations comparable to the Vayda sample from similar water depth (Fig. 5a & b). The seawater $^{231}Pa/^{230}Th$ depth profile derived from Vayda displays a peak constrained by four data points with a maximum value of 1.2 at 2.8 km (Fig. 5c).

Core-top sedimentary $^{231}Pa/^{230}Th$ at all five depth transects display a relatively coherent decreasing trend with increasing water depth over the NADW and mAABW depth range (>1.5 km). In general, core-top $^{231}Pa/^{230}Th$ decreases from values near production ratio (~0.093) at 1.5–2.5 km to ~0.045 at 4.5 km (Fig. 5d). At intermediate water depths (0.5–1.5 km) where the sites are bathed in mAAIW, core-top sedimentary $^{231}Pa/^{230}Th$ are above the production ratio, with higher values at shallower depths, reaching 0.27 at the shallowest site (0.57 km) (Fig. 5d). Within 0.5–1.5 km, the eastern and mid-Atlantic sites seem to exhibit higher core-top $^{231}Pa/^{230}Th$ than the western sites at comparable water depths (Fig. 5d). The core-top sediment samples are of variable ages (1.0–8.8 ka BP) (Rowland et al., 2017), but existing Atlantic sediment core records show that sedimentary $^{231}Pa/^{230}Th$ varies only by a maximum of 0.02 over the range of these core-top ages (Hoffmann et al., 2018; Lippold et al., 2019; Ng et al., 2018). Such uncertainty is smaller than the range of major core-top $^{231}Pa/^{230}Th$ trends observed and described above.

315

316 ### 4.4. Kd and $F_{Th/Pa}$

317 The Log_{10} Kd_{Th}, Log_{10} Kd_{Pa}, and $F_{Th/Pa}$ of paired seawater and core-top sediment samples range from
318 6.7–7.9, 5.8–6.7, and 3.3–14.7 respectively (Fig. 6). Vayda (and Gramberg) depth profiles hint at
319 modest elevations of $F_{Th/Pa}$ (Fig. 6c), Log_{10} Kd_{Th} (Fig. 6a), and potentially Log_{10} Kd_{Pa} (Fig. 6b)
320 between ~2 and 4 km, where heightened seawater dissolved $^{231}Pa/^{230}Th$ has also been observed
321 (Fig. 5c). Unfortunately, the maximum value of the seawater $^{231}Pa/^{230}Th$ at Vayda 2.8 km depth
322 does not have a paired core-top sediment sample and hence does not have corresponding $F_{Th/Pa,}$
323 Log_{10} Kd_{Th} and Log_{10} Kd_{Pa} values. The heightened $F_{Th/Pa}$, Log_{10} Kd_{Th}, and potentially Log_{10} Kd_{Pa} at
324 depth are defined with the three remaining data points from Vayda 2–4 km depths and one data
325 point from Gramberg 2.7 km depth (Fig. 6).
326
327 The lowest $F_{Th/Pa}$ (3.3–5.3) are found at the intermediate depths (0.5–1.5 km) of Carter, Knipovich
328 and Vema (Fig. 6c), where the highest core-top sedimentary $^{231}Pa/^{230}Th$ (0.19–0.27) are observed
329 (Fig. 5d). These low $F_{Th/Pa}$ values fall very close to the endmember $F_{Th/Pa}$ associated with particulate
330 organic matters: 4.9 ± 4.3 (Hayes et al., 2015b) (Fig. 6c). Interestingly, the vertical flux of TOC (Fig.
331 3g) and core-top sediment TOC content (Rowland et al., 2017) (Fig. 3c) indeed are overall higher at
332 the eastern sites (Carter and Knipovich). $F_{Th/Pa}$ at Carter, Knipovich and Vema gradually increase
333 with depth towards values close to the endmember $F_{Th/Pa}$ associated with lithogenics: 10.0 ± 1.3
334 (Hayes et al., 2015b) (Fig. 6c), as vertical flux of lithogenics (Rowland et al., 2017) (Fig. 3h) and
335 core-top sediment lithogenic content (Fig. 3d) are increased at depth.
336
337 A previous modelling study has indicated the likelihood that seafloor sediments reflect ^{231}Pa and
338 ^{230}Th signals from the bottom ~1 km of the overlying water column (Thomas et al., 2006). Given
339 this previous finding, we have adopted the approach following Lippold et al. (2011) to calculate
340 the Log_{10} Kd_{Th}, Log_{10} Kd_{Pa}, and $F_{Th/Pa}$ using interpolated seawater ^{231}Pa and ^{230}Th measurements
341 from 0.5 km (mid-point of 1 km) above the core-top sediment sample sites. Results obtained with
342 this alternative approach are slightly shifted from the original values (Fig. 6), but they do not cause
343 large changes to the major trends described above.
344

345 ## 5. DISCUSSION

346 ### 5.1. Enhanced removal of seawater ^{231}Pa and ^{230}Th at Vayda and Gramberg

Persistently low seawater dissolved ^{231}Pa and ^{230}Th (Rowland et al., 2017) concentrations (Fig. 5a & b), as well as elevated $Log_{10}\ Kd_{Th}$ and $Log_{10}\ Kd_{Pa}$ (Fig. 6a & b) at deep Vayda and Gramberg (~2–4 km) point towards enhanced removal of the isotopes from seawater. The range of $F_{Th/Pa}$ observed here (~10–18, Fig. 6c) is consistent with scavenging of ^{231}Pa and ^{230}Th by Fe-rich particles in hydrothermal plumes or by resuspended sediments dominantly composed of lithogenics and $CaCO_3$ in nepheloid layers (Hayes et al., 2015b). Either of these processes could be viable at this location because the local elevation of deep Vayda-Gramberg seawater $^{231}Pa/^{230}Th$ (Fig. 7b) is similar to the $^{231}Pa/^{230}Th$ signals at hydrothermal vent fields and documented nepheloid layers (Fig. 7a), which have both been associated with a dispersive flux of the relatively soluble ^{231}Pa towards these settings of enhanced scavenging (Hayes et al., 2015a). However, our own transmissometer data from the study area did not show significant elevation in beam attenuation coefficient (Fig. 2c), which would have supported the presence of particles associated with a nepheloid layer or hydrothermal plume (Hayes et al., 2015a). Below we consider these two different scenarios in the wider oceanographic context.

Recent observations have revealed continuous enhanced removal of ^{231}Pa and ^{230}Th from seawater by a horizontally advecting, thick (~1–2 km thick) plume up to 4000 km downstream of an active hydrothermal site (Pavia et al., 2018). Active hydrothermal vents and plumes have been observed at Logatchev (Chavagnac et al., 2008), consistent with the elevated $I_{Fe/Ti}$ estimated for the region (1.7 ± 0.4, Table 1). Vayda and Gramberg seamounts are located ~350–650 km west from the Logatchev hydrothermal field, MAR (Fig. 1). Therefore, even with no active vent at deep Vayda and Gramberg, seawater dissolved ^{231}Pa and ^{230}Th concentrations at these sites (~2–4 km depth) could still be affected by hydrothermal plume advected from the Logatchev hydrothermal sites (~3 km depth), especially in light of evidence for a westward-flowing deep current from the MAR at ~15^{o} N (Lankhorst et al., 2009). The bulk of the particulates including Fe and Mn oxyhydroxides is expected to have settled out of the advecting plume within ~200 km (Pavia et al., 2018) from the Logatchev source, which is consistent with the low beam attenuation coefficient values at deep Vayda (Fig. 2c). However, nanoparticulate and ligand-bound Fe and Mn that would remain suspended for extended period in the advecting plume could act to continue scavenging ^{231}Pa and ^{230}Th along the flow path (Pavia et al., 2018), leading to the low seawater dissolved isotope concentrations (Fig. 5a & b) at deep Vayda and Gramberg (~2–4 km). A small amount of the hydrothermal-sourced nanoparticulate and ligand-bound Fe and Mn might be deposited at

Vayda and Gramberg, and would be masked by the lithogenic Fe oxides in the sediments, which explain the low $I_{Fe/Ti}$ value at deep Gramberg (Fig. 4).

Alternatively, we consider the possibility of transient nepheloid layers that were not detected during our field campaign. Benthic storms are strong bottom current events found to occur in regions with highly energetic sea-surface eddies, and are considered capable of resuspending fine-grained seafloor sediments and generating transient episodes of intense nepheloid activity (Gardner et al., 2017). A correlation between the occurrence of benthic storms, nepheloid layers and sea-surface eddy kinetic energy has been found in the western North Atlantic (Gardner et al., 2018b; Gardner et al., 2017), and temporal variations of nepheloid layers have been linked to short-term changes in seawater ^{231}Pa and ^{230}Th concentrations observed at the Bermuda Atlantic Time Series Station (Anderson et al., 2012). Vayda and Gramberg seamounts are located just north of a region of active eddy formation with high mean kinetic energy due to the retroflection of the North Brazil Current (Aguedjou et al., 2019). Downward propagation of these eddies could lead to episodic formation of nepheloid layers off the seamounts (Gardner et al., 2017). Importantly for this study site, the high bathymetric relief of the seamounts is thought to promote formation of thick (~1–1.5 km thick) nepheloid zones thousands of meters above the abyssal plain (Gardner et al., 2018a; Gardner et al., 2017). Intense nepheloid layers generated by benthic storms are short-lived (up to months) (Gardner et al., 2017), and could have been missed during the CTD transmissometer data collection at Vayda (Fig. 2c). However, the recurring nature of such nepheloid layers (Gardner et al., 2017) could lead to enhanced scavenging of ^{231}Pa and ^{230}Th at deep Vayda and Gramberg (~2–4 km), causing the low seawater concentrations observed in this region (Fig. 5a & b).

With the existing data set, we are not able to distinguish between transient nepheloid layers or hydrothermal scavenging in the removal of seawater dissolved ^{231}Pa and ^{230}Th at deep Vayda and Gramberg. Further constraining the mechanism at work here would require time-series observations of ^{231}Pa, ^{230}Th (Anderson et al., 2012), particle concentration (Gardner et al., 2017), and high-resolution spatial sampling around active vents in the region (Pavia et al., 2018).

5.2. Deep export versus intermediate-depth scavenging of ^{231}Pa

Away from nepheloid layers, hydrothermal settings and margins, new and existing (Luo et al., 2010; Moran et al., 2002) seawater data from the tropical Atlantic (5–15^{o} N, Fig. 7b) and the North

Atlantic GEOTRACES (Hayes et al., 2015a) section (15–40° N, Fig. 7a) generally show decreasing dissolved $^{231}Pa/^{230}Th$ with increasing depth below the mAAIW-NADW water mass boundary at ~1.5 km. This trend, linked to the concave seawater ^{231}Pa and ^{230}Th concentration depth profiles (e.g. Fig. 5a & b), has a complex relationship with the transit time, flow path, and the scavenging history of deep water masses (Hayes et al., 2015a). Meanwhile, our core-top sediment results consistently show $^{231}Pa/^{230}Th$ below the production ratio (0.093) in the deep basin (>2.5 km), with similar values even at sites proximal to settings of enhanced scavenging (deep Vayda and Gramberg, Fig. 8). The widespread observations of core-top sedimentary $^{231}Pa/^{230}Th<0.093$ in the deep basin is most likely driven by a relatively persistent, large-scale control, which is consistent with a net ^{231}Pa export (relative to ^{230}Th) by the overall southward advection of NADW (Bradtmiller et al., 2014; Lippold et al., 2012; Ng et al., 2018; Yu et al., 1996).

In contrast to the deep water situation, our new core-top results together with sediment data from the Caribbean (Lippold et al., 2011) show a large range of sedimentary $^{231}Pa/^{230}Th$ at intermediate depths (0.5–1.5 km) and a broad east-west difference (Fig. 8). The eastern Carter, Knipovich and mid-Atlantic Vema exhibit the highest observed $^{231}Pa/^{230}Th$, well above the production ratio (0.19–0.27), followed by intermediate values observed at Vayda and Gramberg situated just west of the MAR (0.12–0.16), and finally the Caribbean sites showing values close to the production ratio (~0.09). The regional difference is likely to be associated with enhanced scavenging of ^{231}Pa in the eastern and mid-Atlantic sites driven by higher marine primary productivity (Fig. 1) and elevated flux of organics to the sediments (Fig. 3c & g), consistent with the $F_{Th/Pa}$ data (Fig. 6c) of these sites. This finding is also in agreement with a recent modelling study that has highlighted the importance of particulate organic carbon in controlling sedimentary $^{231}Pa/^{230}Th$ in the Atlantic Ocean (Missiaen et al., 2020). However, we argue that enhanced scavenging of ^{231}Pa from the overlying water column is not sufficient to explain $^{231}Pa/^{230}Th>0.093$ (production ratio) observed in the core-top sediments at 0.5–1.5 km depths (Fig. 8), because that would require preferential scavenging of ^{231}Pa over ^{230}Th, which is not consistent with the derived $F_{Th/Pa}$ values of >1 (Fig. 6c). Instead, the high ratios can only be resolved with an additional input of ^{231}Pa relative to ^{230}Th to the intermediate-depth sites.

First we consider the role of mechanisms related to boundary scavenging, although all of our sites are far from the continental margins. Elevated beam attenuation coefficient at the Carter depth transect in the east (Fig. 2c) may be related to lithogenic input from the African continent

(Rowland et al., 2017) and to relatively high levels of marine productivity (NASA Goddard Space Flight Center, 2018 Reprocessing) (Fig. 1), providing some evidence for a potential influence of boundary scavenging. Indeed, there is a broad increase of seawater dissolved $^{231}Pa/^{230}Th$ eastward from 27° W to 22° W at intermediate depths, for example, from 0.65 to 0.90 at 1.5 km (Fig. 7b), consistent with diffusive transport of the more soluble ^{231}Pa towards the African margin driven by boundary scavenging (Hayes et al., 2015a). Given that the transport length scales associated with lateral eddy diffusivity are estimated to be ~800–1300 km for ^{230}Th and ~2750–3080 km for ^{231}Pa (Hayes et al., 2015a), the preferential net diffusive transport due to boundary scavenging could also contribute to the higher core-top sedimentary $^{231}Pa/^{230}Th$ observed at the eastern sites between the 0.5–1.5 km depth range.

It is harder to explain the high $^{231}Pa/^{230}Th$ at the western sites with boundary scavenging, so we assess the role of mAAIW in transporting ^{231}Pa and ^{230}Th at intermediate depths using a simple box model approach adapted from Deng et al. (2014) and Deng et al. (2018). Advection of the isotopes by the mAAIW, M_{Pa} and M_{Th} (dpm/yr), is estimated (Equation 5) based on the meridional transport of this water mass, Q (m^3/yr), derived at 4.5° S and 24.5° N, and the dissolved isotope concentrations previously analysed near those latitudes (Table 3). At intermediate depths, we find 3.2×10^{13} dpm/yr of ^{231}Pa and 4.5×10^{13} dpm/yr of ^{230}Th transported from the South Atlantic into the northern tropical Atlantic, and 0.9×10^{13} dpm/yr of ^{231}Pa and 1.6×10^{13} dpm/yr of ^{230}Th transported out of the northern tropical Atlantic by the northward propagating mAAIW (Fig. 9). The advective transport gives rise to a net accumulation of the isotopes: 2.3×10^{13} dpm/yr of ^{231}Pa and 2.9×10^{13} dpm/yr of ^{230}Th in the northern tropical Atlantic intermediate layer (0.5–1.5 km). The calculated ^{231}Pa and ^{230}Th accumulation is approximately 53 % and 6 % respectively of the isotopes' production within this intermediate layer (Fig. 9), lending support to the role of mAAIW in contributing to an enhanced input of ^{231}Pa relative to ^{230}Th and the high core-top sedimentary $^{231}Pa/^{230}Th$ above the production ratio (>0.093) at the 0.5 –1.5 km depth range across the northern tropical Atlantic sites (Fig. 8).

Equation 5. $M_{Pa} = Q * [^{231}Pa]_d$

$M_{Th} = Q * [^{230}Th]_d$

We also consider a mechanism that relies on the concentration gradient of ^{231}Pa and ^{230}Th in the water column, maintained by the uniform production and the reversible scavenging behaviour of the isotopes in the ocean (Bacon and Anderson, 1982; Nozaki et al., 1987). The increase of

seawater dissolved ^{231}Pa and ^{230}Th with depth (Fig. 5a & b) allows for the possibility of an upward dispersive flux of these isotopes vertically across the concentration gradients to shallower waters via eddy diffusion. At our study sites, the upward dispersive flux of ^{231}Pa and ^{230}Th is expected to be active from ~0.5 to 1.5–2.5 km depth as the isotope concentrations in seawater increase to peak values (Fig. 5a & b). A first estimation of the proposed upward dispersive flux, V (dpm/m^2/yr), is made (Equation 6) based on the average ^{231}Pa and ^{230}Th concentration gradient (assumed linear) across 1 km depth (Fig. 5a & b), dC/dz (dpm/m^4), and vertical eddy diffusivity, κ_v (m^2/yr), which is in the order of 10^2 m^2/yr over most of the ocean interior (Wunsch and Ferrari, 2004). Calculation yields average V of 0.016 dpm/m^2/yr for ^{231}Pa and 0.033 dpm/m^2/yr for ^{230}Th. Given the region's approximate area of 1.8 x 10^{13} m^2, total upward dispersive transport of ^{231}Pa and ^{230}Th across 1 km depth of the northern tropical Atlantic Ocean are estimated to be 2.9 x 10^{11} dpm/yr and 5.9 x 10^{11} dpm/yr respectively, which are small (about two orders of magnitude lower) compared to the horizontal transport of ^{231}Pa and ^{230}Th by mAAIW estimated above (Fig. 9). However, κ_v can be up to two orders of magnitude higher over complex bathymetry such as the seamounts and MAR at the study sites (Fig. 1), which allows for the possibility of upward dispersive transport to be significant at our sites, contributing to an additional input of the more soluble ^{231}Pa relative to ^{230}Th to shallower water depths. The plausibility of this mechanism, and its potential significance on the vertical redistribution of ^{231}Pa and ^{230}Th especially in regions of enhanced vertical diffusivity (seamounts, mid-ocean ridges) across the global ocean require further testing in future studies.

Equation 6. $V = \kappa_v * dC/dz$

6. Conclusions

A total of 20 seawater and 20 core-top ^{231}Pa and ^{230}Th analyses along five depth transects (Carter, Knipovich, Vema, Vayda and Gramberg) across the northern tropical Atlantic open ocean, with 18 seawater-sediment pairs from nearby sites, reveal a coherent decrease in sedimentary ^{231}Pa/^{230}Th from all five depth transects and seawater dissolved ^{231}Pa/^{230}Th from Carter, Knipovich and Vema below 1.5 km depth. In contrast, seawater results from Vayda and Gramberg show persistently low dissolved ^{231}Pa concentration, ^{230}Th concentration, and elevated dissolved ^{231}Pa/^{230}Th, Kd_{Th}, Kd_{Pa} and $F_{Th/Pa}$ at 2–4 km depths. These observations suggest enhanced removal of ^{231}Pa, ^{230}Th and a dispersive flux of ^{231}Pa towards deep Vayda and Gramberg. Enhanced scavenging of the isotopes at these sites could be caused either by nearby hydrothermal vents or by episodic formation of transient nepheloid layers at the seamounts.

Meanwhile, sedimentary $^{231}Pa/^{230}Th$ across the deep (>2.5 km) northern tropical Atlantic are consistently below the production ratio, with similarly low values observed even at sites proximal to settings of enhanced scavenging. This observation supports the dominance of the ^{231}Pa-export signal in the deep Atlantic associated with the overall southward advection of NADW. In contrast, at intermediate depths (0.5–1.5 km), core-top results show pronounced elevation of sedimentary $^{231}Pa/^{230}Th$ above the production ratio, with higher values at the eastern and mid-Atlantic sites (Carter, Knipovich and Vema). In light of the paired seawater $^{231}Pa/^{230}Th$ and $F_{Th/Pa}$ data, these observations could be explained with an additional input of ^{231}Pa to the intermediate depths, enhanced ^{231}Pa scavenging at the eastern and mid-Atlantic sites, and/or the influence of boundary scavenging near the eastern margin. Greater ^{231}Pa scavenging might be related to elevated levels of marine primary productivity inferred at Carter, Knipovich and Vema, while the additional ^{231}Pa input could be partly maintained by mAAIW advection, and partly sourced from depth via an upward dispersive flux. The proposed upward dispersive flux is expected to have a significant magnitude at settings of enhanced vertical diffusivity such as seamounts and mid-ocean ridges, and should be considered in the evaluation of the processes that contribute to the cycling of ^{231}Pa and ^{230}Th, and the distribution of $^{231}Pa/^{230}Th$ in the ocean.

Acknowledgements

We would like to express our gratitude to the European Research Council for providing support to this study. The contribution of Jerry McManus to this research was supported in part by US-NSF award number AGS 16-35019. We appreciate the help and advice from Christopher Coath, Katherine Adena, Tim Elliot and Carolyn Taylor from the Bristol Isotope Group, and Maureen Auro from WHOI in setting up the sediment and seawater $^{231}Pa/^{230}Th$ analytical protocol at the UoB. Great thanks to the scientists and crew of JC094 for their assistance in collection of sediment and seawater samples from the tropical Atlantic Ocean. We are also grateful to Suzanne Maclachlan and BOSCORF for providing support in sediment core scanning operation. Sincere thanks to Sifan Gu and Zhengyu Liu for insightful discussions.

Data statement

The data reported in this paper are listed in the Supplementary Information and will be archived in Pangaea database.

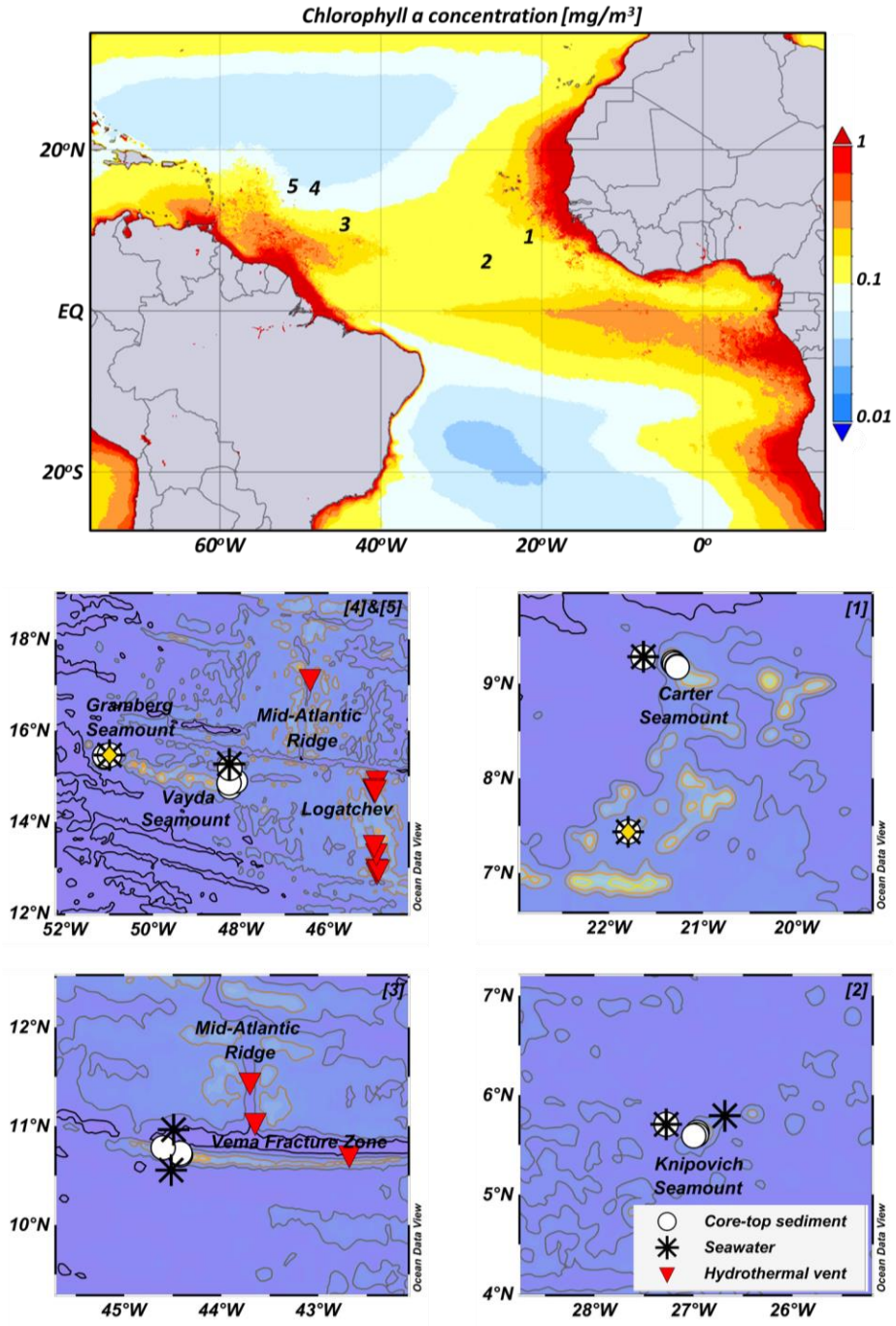

Figure 1. Site maps showing the locations of core-top sediment and seawater samples. The sample sites consist mainly of five labelled depth transects: [1] Carter, [2] Knipovich, [3] Vema, [4] Vayda, and [5] Gramberg. Surface ocean chlorophyll concentrations plotted in log scale on the top regional map are long-term averages of monthly satellite (MODIS-Aqua) data (NASA Goddard Space Flight Center, 2018 Reprocessing) over year 2002–2013 derived using the Giovanni online data system (Acker and Leptoukh, 2007). Individual local maps focusing on the respective coordinates of depth transects [1]–[5] have contour lines drawn to indicate water depths (black, grey, brown, orange and yellow lines mark 5 km, 4 km, 3 km, 2 km and 1 km depths respectively). Based on historical observations published on the InterRidge Vents Database (Beaulieu et al., 2013) Ver. 3.4 (accessed online on 22 June 2020), potentially active hydrothermal vent fields in proximity to the sample sites are plotted on the local maps. Yellow diamonds mark the sediment cores used to derive Fe/Ti for Gramberg and Carter sites (Fig. 4) as a tracer of hydrothermal activity. The local maps were generated using the Ocean Data View (ODV) program (Schlitzer, 2012).

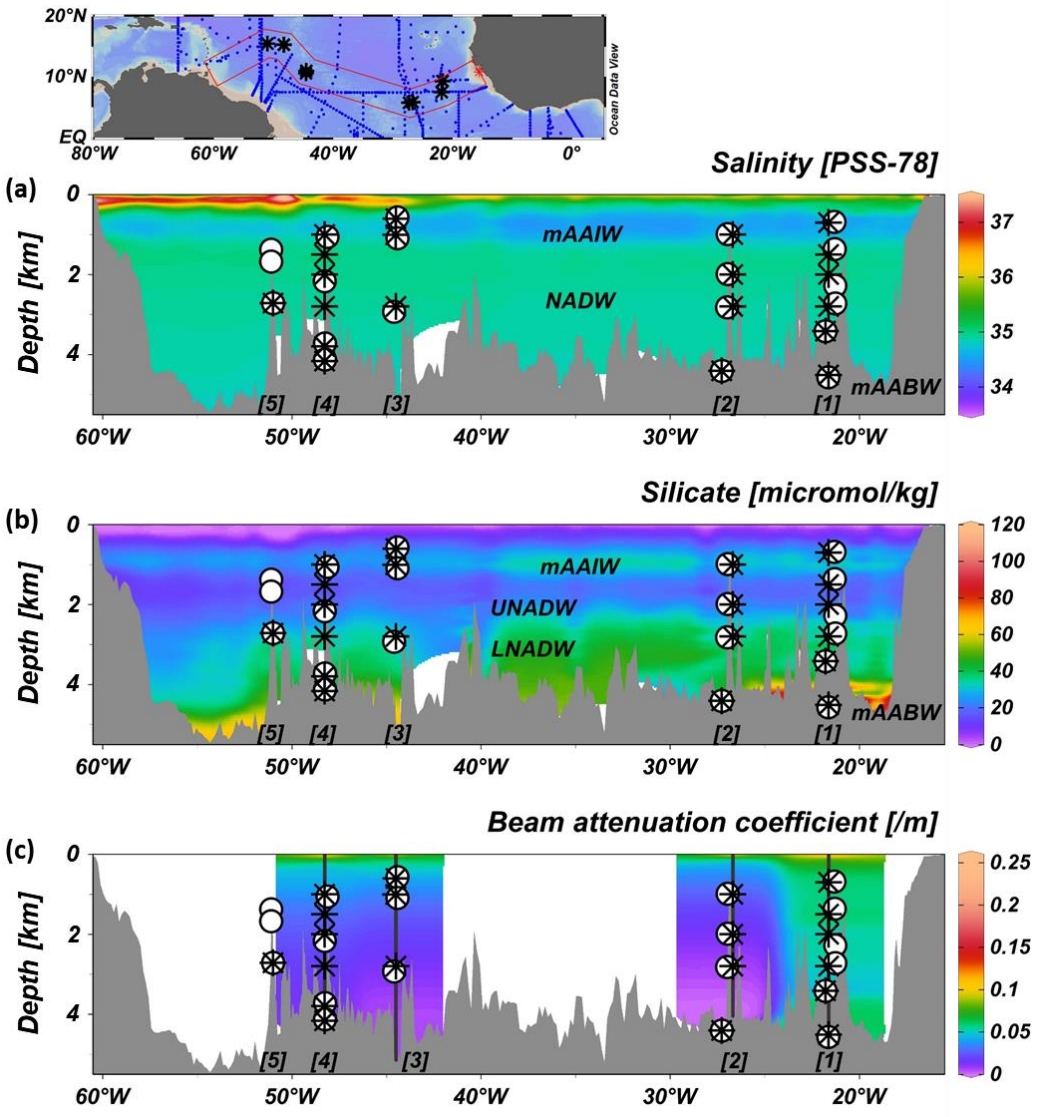

Figure 2. Depth sections showing seawater properties at the northern tropical Atlantic. **(a)** Salinity, **(b)** Silicate concentration, and **(c)** Beam attenuation coefficient. Salinity and silicate concentration data consist of measurements of seawater samples obtained from the JC094 cruise (Robinson, 2014) and those published on the GLODAP database (Key et al., 2004), which are marked by the black stars and blue dots respectively on the map. Black lines in (c) mark where the beam attenuation coefficient data were collected from during the JC094 cruise, at depth resolution greater than 1 m. Red line drawn on the map defines the boundary of the depth sections. The symbols (defined in Fig. 1) plotted atop the depth sections mark the sample sites from depth transects labelled [1]–[5]. Bathymetry shown in dark grey is from GEBCO 30 arc-second grid (Weatherall et al., 2015), and sites may appear to be 'below' or 'floating above' the seafloor because they are superimposed on a representative section across the Atlantic, rather than the overlying bathymetry measured at the actual sites. This figure was generated using the Ocean Data View (ODV) program (Schlitzer, 2012).

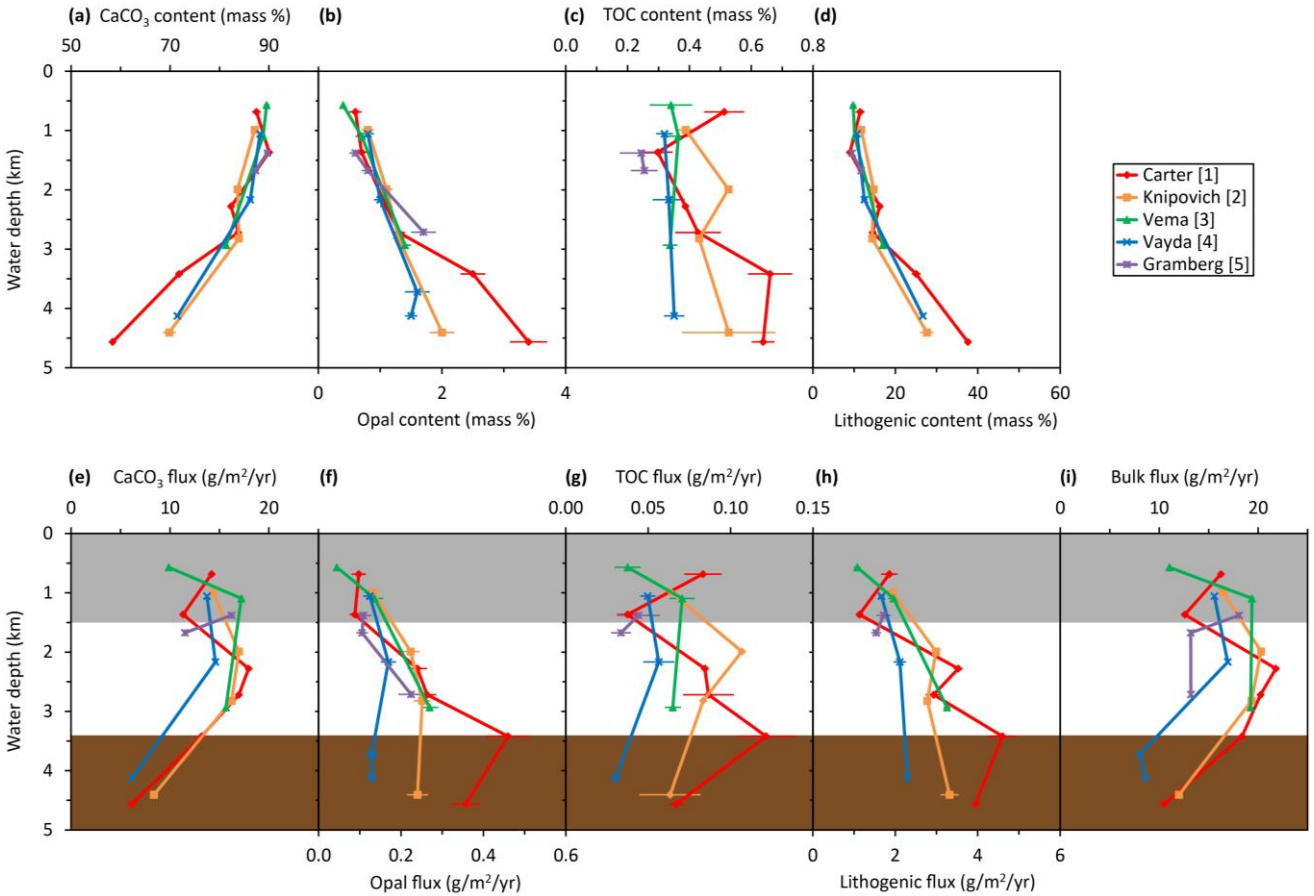

Figure 3. Core-top sediment composition at the study sites and vertical sediment fluxes derived using the ^{230}Th-normalisation method (Rowland et al., 2017). Core-top sediment **(a)** $CaCO_3$ content, **(b)** opal content, **(c)** total organic carbon (TOC) content, and **(d)** lithogenic content; Vertical **(e)** $CaCO_3$ flux, **(f)** opal flux, **(g)** TOC flux, **(h)** lithogenic flux, and **(i)** bulk sediment flux. Error bars represent 95 % confidence interval. The ^{230}Th-normalised fluxes from ~1.5–3.5 km depth most likely represent the best estimates of vertical sediment fluxes along the depth transects (Rowland et al., 2017). This is because the use of ^{230}Th-normalisation method in the study area is subject to greater uncertainties above ~1.5 km depth (grey bar) (Rowland et al., 2017) partly due to the low ^{230}Th inventories at shallower water (Costa et al., 2020), and greater uncertainties below ~3.5 km depth (brown bar) as a result of $CaCO_3$ dissolution, sediment redistribution and Th advection at depth (Costa et al., 2020; Rowland et al., 2017).

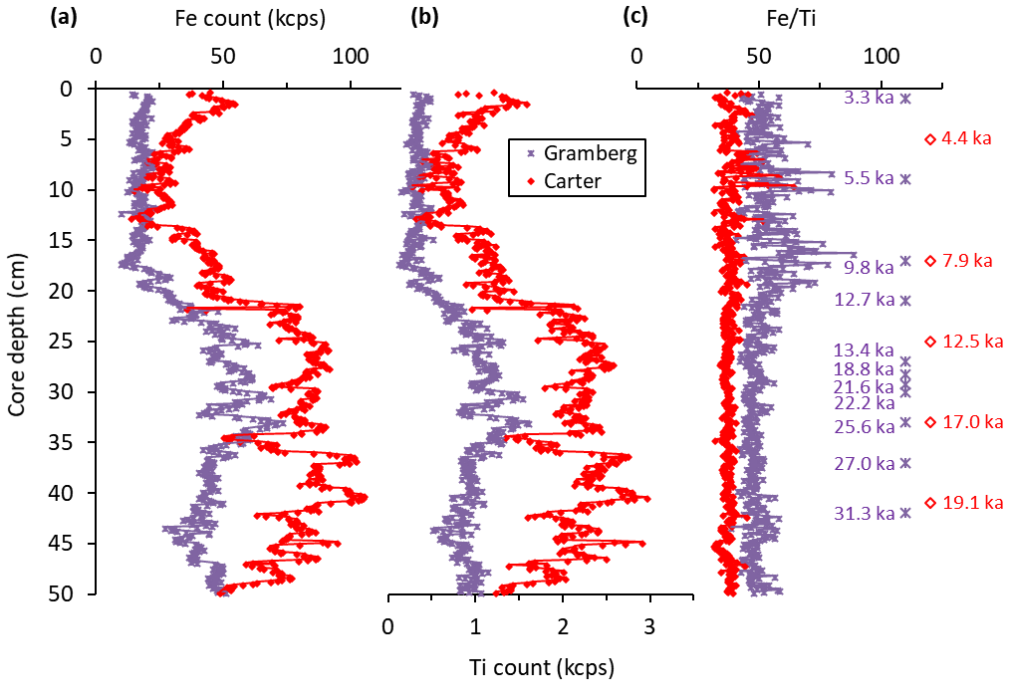

576
577 **Figure 4.** ITRAX core scanner Fe and Ti data for JC094-GVY14 (Gramberg) and JC094-GVY01 (Carter). **(a)** Fe
578 data in kilo-counts per second (kcps), **(b)** Ti data, and **(c)** Fe/Ti ratio focusing on the top 50 cm of the
579 sediment cores. Data was generated at 0.1 cm depth resolution. Lines display 5-point weighted running
580 mean of the data. Empty symbols at the far right mark the core depths at which chronological tie-points
581 were established with ^{14}C method, and the annotations indicate the corresponding derived (calendar) ages
582 (Ng et al., 2018).

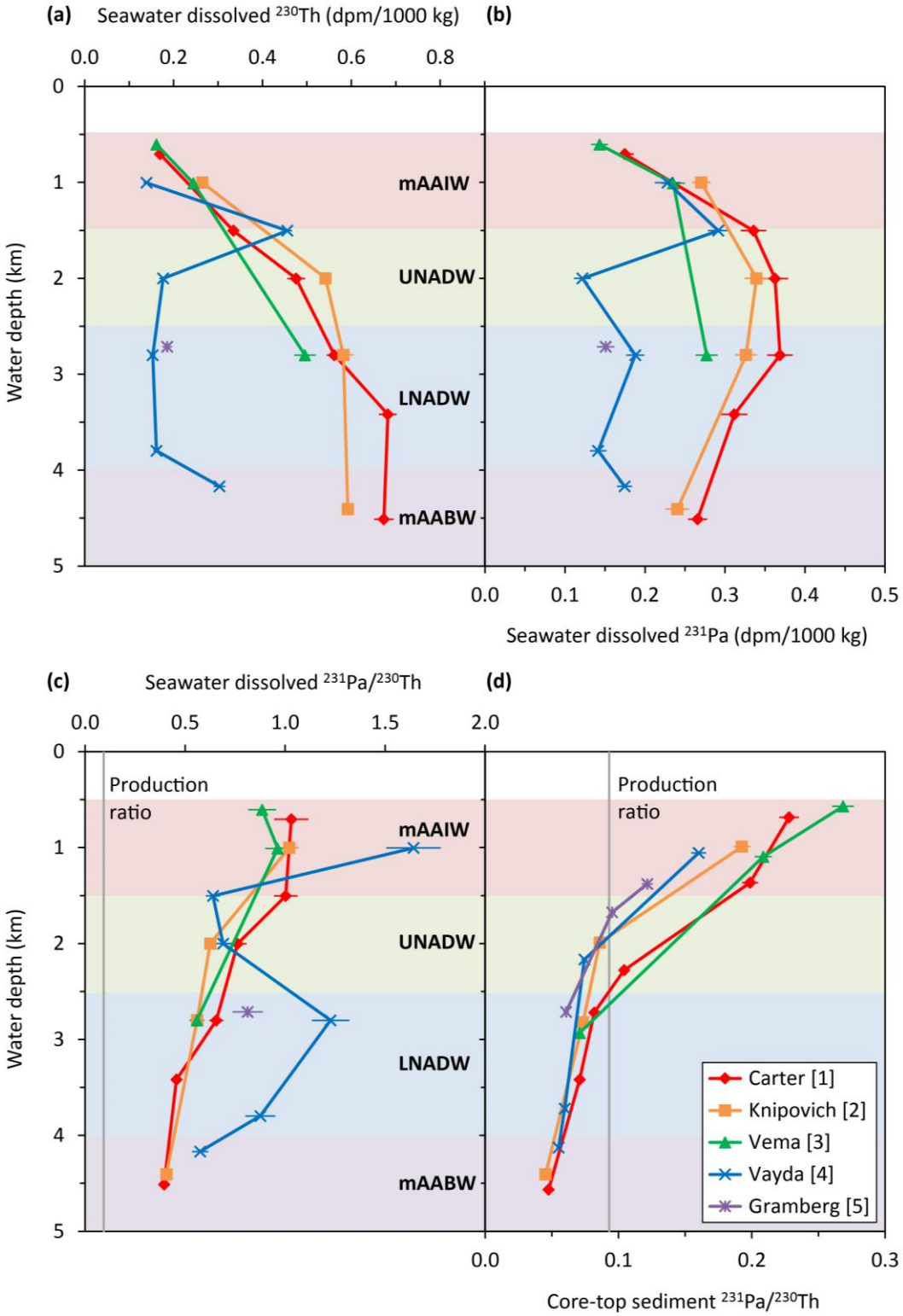

Figure 5. Tropical Atlantic ^{231}Pa and ^{230}Th data. Depth profiles of seawater dissolved **(a)** ^{230}Th concentration (Rowland et al., 2017), **(b)** ^{231}Pa concentration (new results), **(c)** ^{231}Pa/^{230}Th (new results); and core-top sediment **(d)** ^{231}Pa/^{230}Th (new results). Data are plotted as five labelled depth transects from the localities indicated in Fig. 1. Shaded areas in red, green, blue and purple indicate the approximate water depth ranges where the following water masses are observed: mAAIW, UNADW, LNADW and mAABW respectively (Fig. 2). Error bars represent 2 S.E.M. analytical uncertainties.

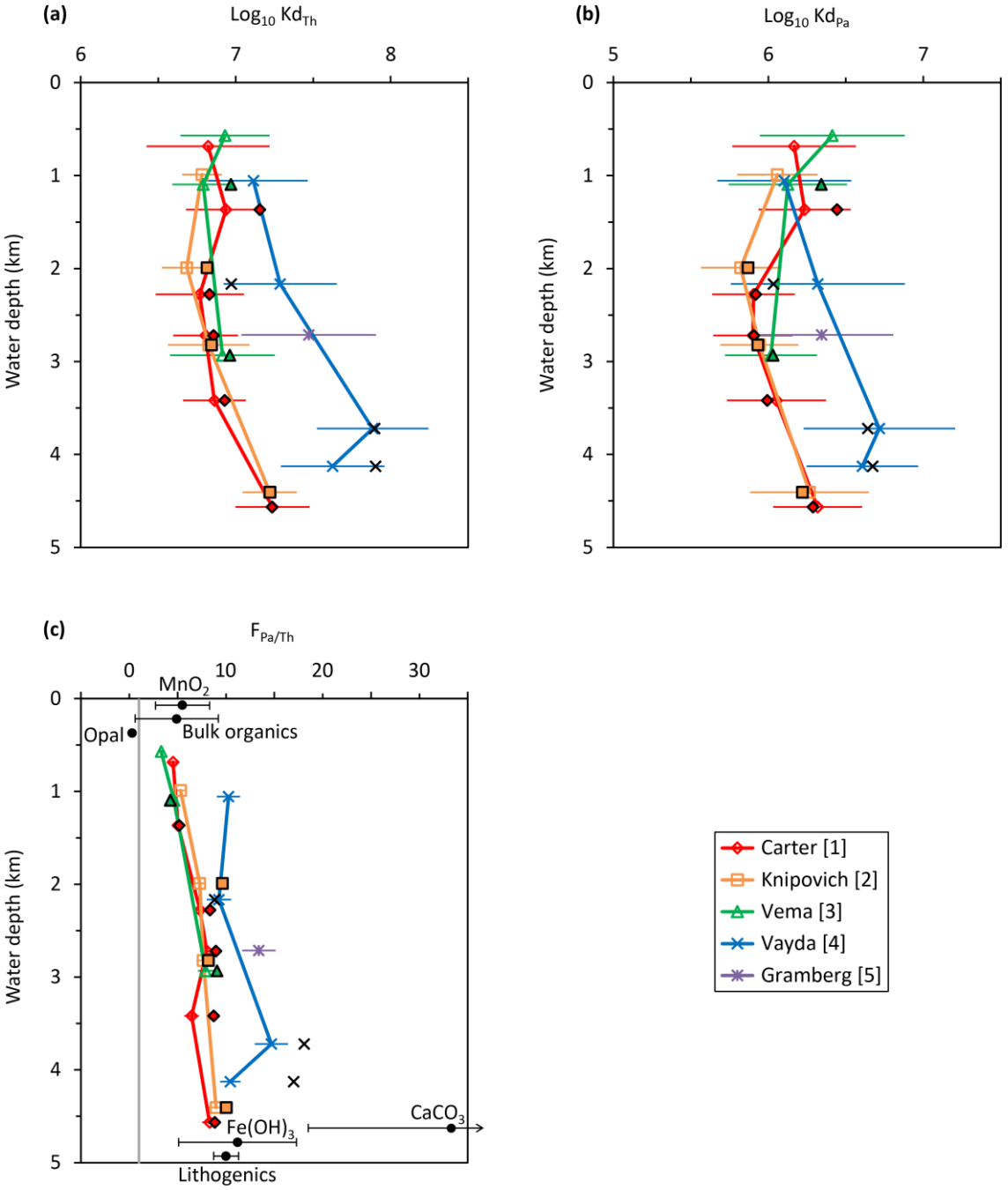

591
592 **Figure 6.** Pa and Th distribution coefficients and fractionation factor. **(a)** Log_{10} Kd_{Th}, **(b)** Log_{10} Kd_{Pa}, and **(c)**
593 $F_{Pa/Th}$. Empty symbols and solid lines are results calculated based on paired seawater and core-top samples
594 that were acquired from nearby sites (with water depth differences of no greater than 0.28 km), and error
595 bars represent 95 % confidence interval. Filled symbols with black outline are results calculated using
596 interpolated seawater data, assuming that sedimentary ^{231}Pa and ^{230}Th signals are derived from the bottom
597 ~1 km of the overlying water column (Lippold et al., 2011; Thomas et al., 2006). The latter approach does
598 not yield Log_{10} Kd_{Th}, Log_{10} Kd_{Pa} and $F_{Pa/Th}$ for the shallowest site of each depth transect, which would
599 otherwise require extrapolation of seawater ^{231}Pa and ^{230}Th measurements. The vertical grey line marks
600 $F_{Pa/Th}$ = 1 which indicates no fractionation between the two isotopes by scavenging. The annotations
601 indicate the endmember $F_{Pa/Th}$ for $CaCO_3$, lithogenics, organic matters, $Fe(OH)_3$ and MnO_2 derived by Hayes
602 et al. (2015b), and endmember $F_{Pa/Th}$ for biogenic opal derived by Chase et al. (2002).

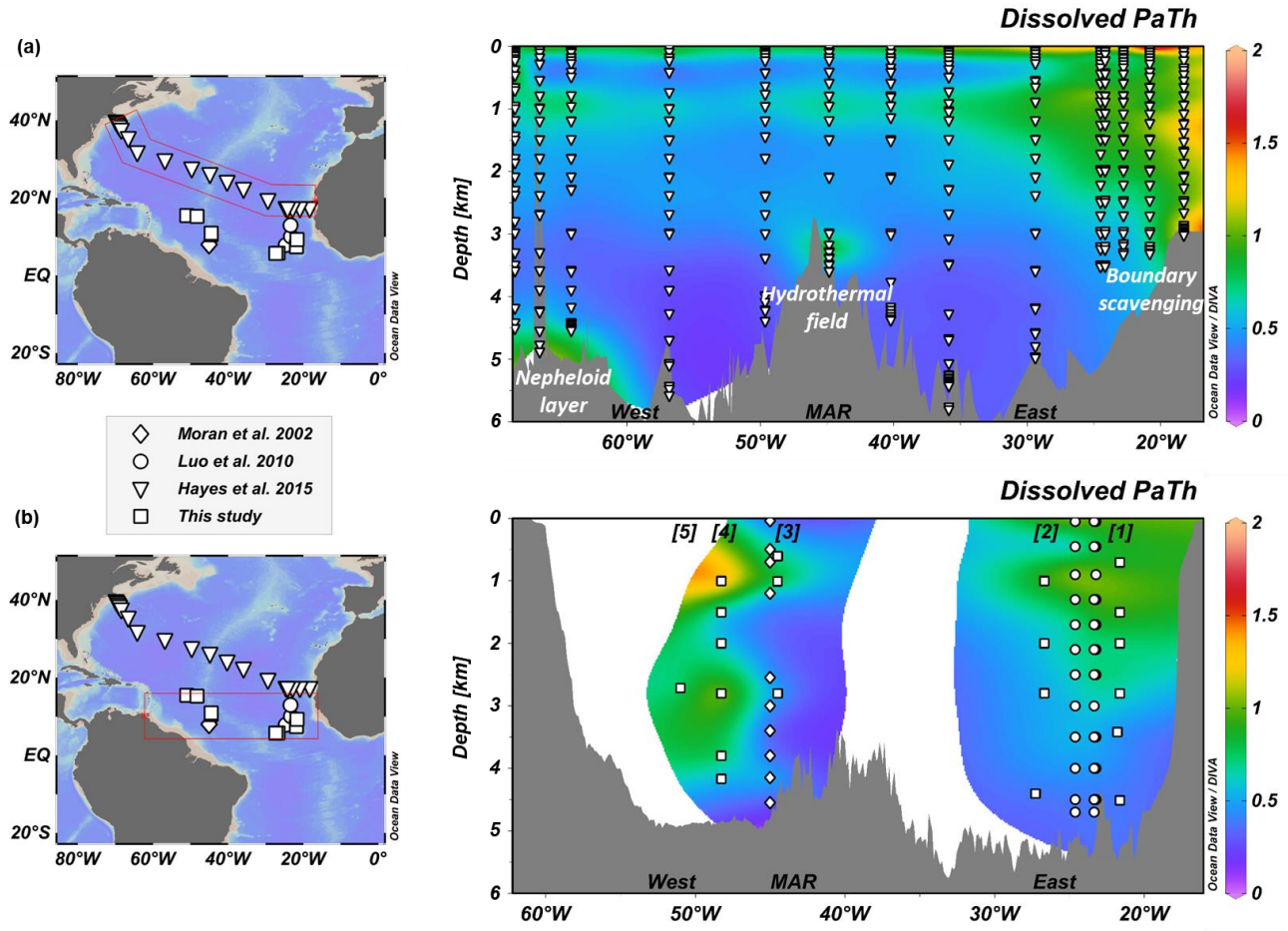

Figure 7. East-West depth sections of new and published seawater dissolved $^{231}Pa/^{230}Th$. **(a)** North Atlantic and **(b)** tropical Atlantic depth sections. The colour maps were developed by applying the Data-Interpolating Variational Analysis (DIVA) method on the individual dissolved $^{231}Pa/^{230}Th$ data using ODV (Schlitzer, 2012). Red line drawn on the map defines the boundary of the depth sections. Number 1–5 labelled on the depth sections, defined in Fig. 1, indicate the depth transects where the sample sites of this study are located.

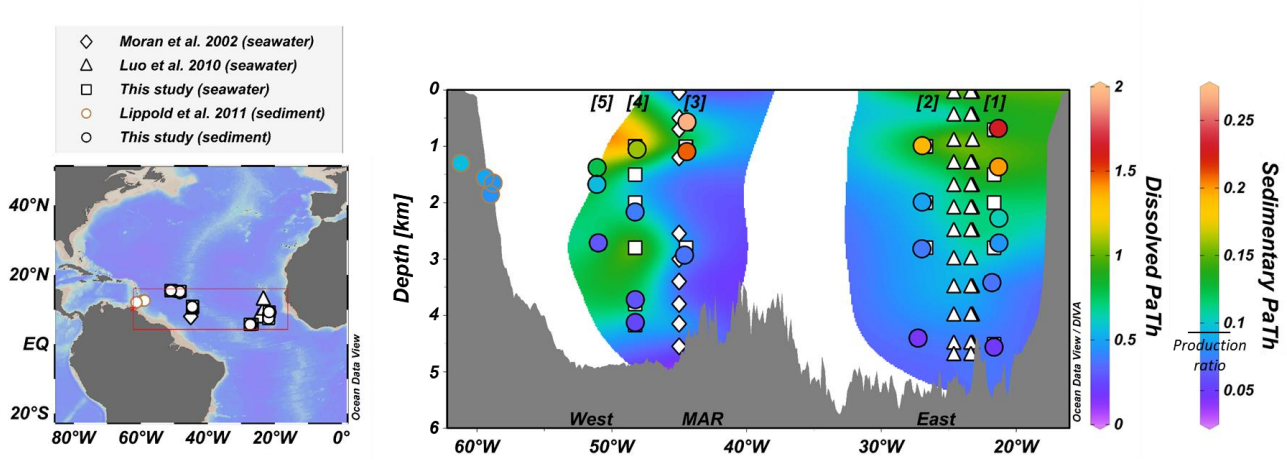

Figure 8. Compilation of new and published seawater and core-top $^{231}Pa/^{230}Th$ from the northern tropical Atlantic. The East-West depth section of seawater dissolved $^{231}Pa/^{230}Th$ data is plotted in the same way as described in Fig. 7b. The core-top sedimentary $^{231}Pa/^{230}Th$ data is plotted overlain the seawater data as coloured dots. Number 1–5 labelled on the depth sections, defined in Fig. 1, indicate the depth transects where the sample sites of this study are located. Bathymetry shown in dark grey is from GEBCO 30 arc-second grid (Weatherall et al., 2015), and core-top sediment sites may appear to be 'below' or 'floating above' the seafloor because they are superimposed on a representative section across the Atlantic, rather than the overlying bathymetry measured at the actual sites.

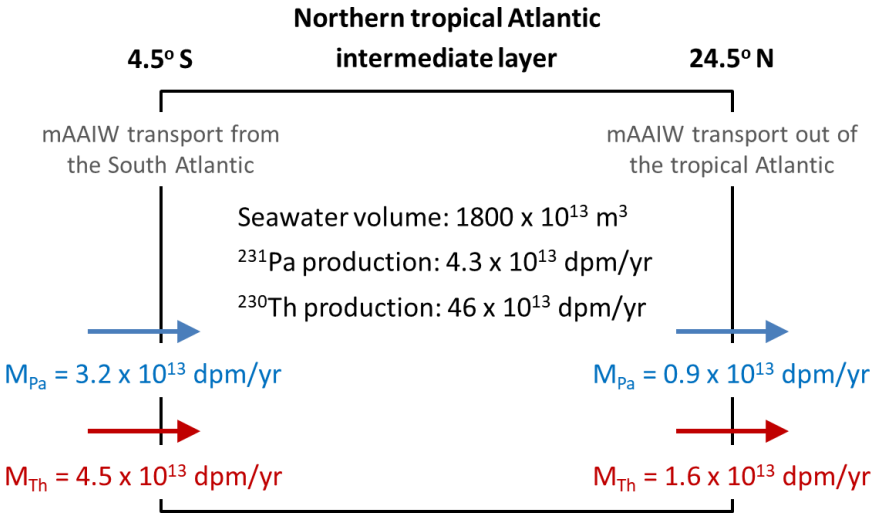

Figure 9. Schematic showing the horizontal transport of ^{231}Pa and ^{230}Th by mAAIW advection across the intermediate depths of the northern tropical Atlantic Ocean. Production rates of ^{231}Pa and ^{230}Th are 0.00237 dpm/m^3/yr and 0.0257 dpm/m^3/yr respectively (Deng et al., 2018).

623 **Table 1.** Calculation of $I_{Fe/Ti}$ using Fe/Ti data from identified or potential hydrothermal settings, and Fe/Ti
624 data from background settings away from hydrothermal sites (Equation 2).

Identified/potential hydrothermal site	Background site	Reference	Material	$I_{Fe/Ti}$	+/-
[a]Gramberg (GVY14), Atlantic	Carter (GVY01), Atlantic	This study	Sediment	1.29	0.34
[a]Hook Ridge (MC16), Antarctica	Antarctic Peninsula shelf (MC1/2/3)	(Aquilina et al., 2014)	Sediment	2.9	0.1
Rainbow hydrothermal field, Atlantic	Atlantic abyssal plain (BOFS)	(Cave et al., 2002)	Sediment	3.3	1.5
Logatchev hydrothermal field, Atlantic	Atlantic abyssal plain (BOFS)	(Chavagnac et al., 2008)	Sediment	1.7	0.4
TAG hydrothermal field, Atlantic	Atlantic open ocean interior	(Ohnemus and Lam, 2015)	Seawater particulate	>3	-

625 [a]$I_{Fe/Ti}$ was calculated based on the Fe/Ti data from the top ~1 cm of the sediment cores.

Table 2. Comparison of sediment and seawater standard ^{231}Pa and ^{230}Th measured in this study with reported values. Measured values are long-term averages (and 95 % confidence interval) of repeat analysis of the sediment and seawater standards over the duration of this study (April 2014–June 2015).

Standard	Isotope	Number of replicates	Measured value	Reference value	Reference
Siliceous ooze	^{231}Pa	10	1.24 ± 0.04 dpm/g	1.25 ± 0.07 dpm/g	(Anderson et al., 2012)
	^{230}Th	10	5.48 ± 0.09 dpm/g	5.53 ± 0.22 dpm/g	
Seawater standard	^{231}Pa	7	6.35 ± 0.19 dpm/kg	6.26 ± 0.08 dpm/kg	[a](Auro et al., 2012)
	^{230}Th	11	16.1 ± 0.4 dpm/kg	15.8 ± 0.2 dpm/kg	

[a]The artificial seawater standard was made such that ~0.1–0.2 ml of the standard solution had equivalent amounts of Pa and Th isotopes as those in 4–5 L of a typical seawater sample. The seawater standard was calibrated along with the analysis of GEOTRACES inter-laboratory calibration seawater standard (Anderson et al., 2012) at the Woods Hole Oceanographic Institution laboratory following the analytical procedures detailed in (Auro et al., 2012).

Table 3. Parameters used in the evaluation of the mAAIW transport of ^{231}Pa and ^{230}Th at intermediate depths.

Latitude	Q (m^3/yr)	Reference	$[^{231}Pa]_d$ (dpm/m^3)	$[^{230}Th]_d$ (dpm/m^3)	Reference/ Station
24.5° N	4.7×10^{13}	(Fu et al., 2018)	0.20	0.35	(Deng et al., 2014) JC057-18
4.5° S	16×10^{13}	(Vanicek and Siedler, 2002)	0.20	0.28	(Hayes et al., 2015a) GT11-14

References

Acker, J.G., Leptoukh, G., 2007. Online Analysis Enhances Use of NASA Earth Science Data. Eos Trans. AGU 88, 14-17. doi:10.1029/2007EO020003.

Aguedjou, H.M.A., Dadou, I., Chaigneau, A., Morel, Y., Alory, G., 2019. Eddies in the Tropical Atlantic Ocean and Their Seasonal Variability. Geophys Res Lett 46, 12156-12164. doi:10.1029/2019gl083925.

Anderson, R.F., Ali, S., Bradtmiller, L.I., Nielsen, S.H.H., Fleisher, M.Q., Anderson, B.E., Burckle, L.H., 2009. Wind-Driven Upwelling in the Southern Ocean and the Deglacial Rise in Atmospheric CO2. Science 323, 1443-1448. doi:10.1126/science.1167441.

Anderson, R.F., Bacon, M.P., Brewer, P.G., 1983a. Removal of Th-230 and Pa-231 at Ocean Margins. Earth Planet Sc Lett 66, 73-90. doi:10.1016/0012-821x(83)90127-9.

Anderson, R.F., Bacon, M.P., Brewer, P.G., 1983b. Removal of Th-230 and Pa-231 from the Open Ocean. Earth Planet Sc Lett 62, 7-23. doi:10.1016/0012-821x(83)90067-5.

Anderson, R.F., Fleer, A.P., 1982. Determination of Natural Actinides and Plutonium in Marine Particulate Material. Anal Chem 54, 1142-1147. doi:10.1021/Ac00244a030.

Anderson, R.F., Fleisher, M.Q., Robinson, L.F., Edwards, R.L., Hoff, J.A., Moran, S.B., van der Loeff, M.R., Thomas, A.L., Roy-Barman, M., Francois, R., 2012. GEOTRACES intercalibration of Th-230, Th-232, Pa-231, and prospects for Be-10. Limnol. Oceanogr. Meth. 10, 179-213. doi:10.4319/lom.2012.10.179.

Aquilina, A., Homoky, W.B., Hawkes, J.A., Lyons, T.W., Mills, R.A., 2014. Hydrothermal sediments are a source of water column Fe and Mn in the Bransfield Strait, Antarctica. Geochim Cosmochim Ac 137, 64-80. doi:10.1016/j.gca.2014.04.003.

Auro, M.E., Robinson, L.F., Burke, A., Bradtmiller, L.I., Fleisher, M.Q., Anderson, R.F., 2012. Improvements to 232-thorium, 230-thorium, and 231-protactinium analysis in seawater arising from GEOTRACES intercalibration. Limnol. Oceanogr. Meth. 10, 464-474. doi:10.4319/lom.2012.10.464.

Bacon, M.P., 1988. Tracers of Chemical Scavenging in the Ocean - Boundary Effects and Large-Scale Chemical Fractionation. Philos T R Soc A 325, 147-160. doi:10.1098/rsta.1988.0048.

Bacon, M.P., Anderson, R.F., 1982. Distribution of Thorium Isotopes between Dissolved and Particulate Forms in the Deep-Sea. J Geophys Res-Oc Atm 87, 2045-2056. doi:10.1029/Jc087ic03p02045.

Beaulieu, S.E., Baker, E.T., German, C.R., Maffei, A., 2013. An authoritative global database for active submarine hydrothermal vent fields. Geochemistry, Geophysics, Geosystems 14, 4892-4905. doi:10.1002/2013GC004998.

Bourne, M.D., Thomas, A.L., Mac Niocaill, C., Henderson, G.M., 2012. Improved determination of marine sedimentation rates using Th-230(xs). Geochem Geophy Geosy 13, Q09017. doi:10.1029/2012gc004295.

Bradtmiller, L.I., Anderson, R.F., Fleisher, M.Q., Burckle, L.H., 2006. Diatom productivity in the equatorial Pacific Ocean from the last glacial period to the present: A test of the silicic acid leakage hypothesis. Paleoceanography 21, PA4201. doi:10.1029/2006pa001282.

Bradtmiller, L.I., Anderson, R.F., Fleisher, M.Q., Burckle, L.H., 2009. Comparing glacial and Holocene opal fluxes in the Pacific sector of the Southern Ocean. Paleoceanography 24, PA2214. doi:10.1029/2008pa001693.

Bradtmiller, L.I., McManus, J.F., Robinson, L.F., 2014. 231Pa/230Th evidence for a weakened but persistent Atlantic meridional overturning circulation during Heinrich Stadial 1. Nat Commun 5, 5817. doi:10.1038/ncomms6817.

Cave, R.R., German, C.R., Thomson, J., Nesbitt, R.W., 2002. Fluxes to sediments underlying the Rainbow hydrothermal plume at 36° 14′ N on the Mid-Atlantic Ridge. Geochim Cosmochim Ac 66, 1905-1923. doi:10.1016/S0016-7037(02)00823-2.

Chase, Z., Anderson, R.F., Fleisher, M.Q., Kubik, P.W., 2002. The influence of particle composition and particle flux on scavenging of Th, Pa and Be in the ocean. Earth Planet Sc Lett 204, 215-229. doi:10.1016/S0012-821x(02)00984-6.

Chavagnac, V., Lair, M., Milton, J.A., Lloyd, A., Croudace, I.W., Palmer, M.R., Green, D.R.H., Cherkashev, G.A., 2008. Tracing dust input to the Mid-Atlantic Ridge between 14° 45′ N and 36° 14′ N: Geochemical and Sr isotope study. Mar Geol 247, 208-225. doi:10.1016/j.margeo.2007.09.003.

Costa, K.M., Hayes, C.T., Anderson, R.F., Pavia, F.J., Bausch, A., Deng, F., Dutay, J.-C., Geibert, W., Heinze, C., Henderson, G., Hillaire-Marcel, C., Hoffmann, S., Jaccard, S.L., Jacobel, A.W., Kienast, S.S., Kipp, L., Lerner, P., Lippold, J., Lund, D., Marcantonio, F., McGee, D., McManus, J.F., Mekik, F., Middleton, J.L., Missiaen, L., Not, C., Pichat, S., Robinson, L.F., Rowland, G.H., Roy-Barman, M., Tagliabue, A., Torfstein, A., Winckler, G., Zhou, Y., 2020. 230Th Normalization: New Insights on an Essential Tool for Quantifying Sedimentary Fluxes in the Modern and Quaternary Ocean. Paleoceanography and Paleoclimatology 35, e2019PA003820. doi:10.1029/2019pa003820.

Costa, K.M., Jacobel, A.W., McManus, J.F., Anderson, R.F., Winckler, G., Thiagarajan, N., 2017. Productivity patterns in the equatorial Pacific over the last 30,000 years. Global Biogeochem Cy 31, 850-865. doi:10.1002/2016GB005579.

Deng, F., Henderson, G.M., Castrillejo, M., Perez, F.F., Steinfeldt, R., 2018. Evolution of 231Pa and 230Th in overflow waters of the North Atlantic. Biogeosciences 15, 7299-7313. doi:10.5194/bg-15-7299-2018.

Deng, F.F., Thomas, A.L., Rijkenberg, M.J.A., Henderson, G.M., 2014. Controls on seawater Pa-231, Th-230 and Th-232 concentrations along the flow paths of deep waters in the Southwest Atlantic. Earth Planet Sc Lett 390, 93-102. doi:10.1016/j.epsl.2013.12.038.

Estapa, M.L., Breier, J.A., German, C.R., 2015. Particle dynamics in the rising plume at Piccard Hydrothermal Field, Mid-Cayman Rise. Geochemistry, Geophysics, Geosystems 16, 2762-2774. doi:10.1002/2015GC005831.

Frank, M., Jeandel, C., Anderson, R.F., Henderson, G., Francois, R., Sharma, M., 2003. GEOTRACES: Studying the global marine biogeochemistry of trace elements and isotopes. Eos, Transactions American Geophysical Union 84, 327-330. doi:10.1029/2003eo340006.

Fu, Y., Karstensen, J., Brandt, P., 2018. Atlantic Meridional Overturning Circulation at 14.5° N in 1989 and 2013 and 24.5° N in 1992 and 2015: volume, heat, and freshwater transports. Ocean Sci. 14, 589-616. doi:10.5194/os-14-589-2018.

Gardner, W.D., Jo Richardson, M., Mishonov, A.V., Biscaye, P.E., 2018a. Global comparison of benthic nepheloid layers based on 52 years of nephelometer and transmissometer measurements. Progress in Oceanography 168, 100-111. doi:10.1016/j.pocean.2018.09.008.

Gardner, W.D., Richardson, M.J., Mishonov, A.V., 2018b. Global assessment of benthic nepheloid layers and linkage with upper ocean dynamics. Earth Planet Sc Lett 482, 126-134. doi:10.1016/j.epsl.2017.11.008.

Gardner, W.D., Tucholke, B.E., Richardson, M.J., Biscaye, P.E., 2017. Benthic storms, nepheloid layers, and linkage with upper ocean dynamics in the western North Atlantic. Mar Geol 385, 304-327. doi:10.1016/j.margeo.2016.12.012.

Geibert, W., Usbeck, R., 2004. Adsorption of thorium and protactinium onto different particle types: Experimental findings. Geochim Cosmochim Ac 68, 1489-1501. doi:10.1016/j.gca.2003.10.11.

Grenier, M., François, R., Soon, M., Rutgers van der Loeff, M., Yu, X., Valk, O., Not, C., Moran, S.B., Edwards, R.L., Lu, Y., Lepore, K., Allen, S.E., 2019. Changes in Circulation and Particle Scavenging in the Amerasian Basin of the Arctic Ocean over the Last Three Decades Inferred from the Water Column Distribution of Geochemical Tracers. Journal of Geophysical Research: Oceans 124, 9338-9363. doi:10.1029/2019jc015265.

Gu, S., Liu, Z., 2017. 231Pa and 230Th in the ocean model of the Community Earth System Model (CESM1.3). Geosci. Model Dev. 10, 4723-4742. doi:10.5194/gmd-10-4723-2017.

Guo, L.D., Chen, M., Gueguen, C., 2002. Control of Pa/Th ratio by particulate chemical composition in the ocean. Geophys Res Lett 29. doi:10.1029/2002gl015666.

Hayes, C.T., Anderson, R.F., Fleisher, M.Q., Huang, K.F., Robinson, L.F., Lu, Y.B., Cheng, H., Edwards, R.L., Moran, S.B., 2015a. Th-230 and Pa-231 on GEOTRACES GA03, the US GEOTRACES North Atlantic transect, and implications for modern and paleoceanographic chemical fluxes. Deep-Sea Res Pt Ii 116, 29-41. doi:10.1016/j.dsr2.2014.07.007.

Hayes, C.T., Anderson, R.F., Fleisher, M.Q., Vivancos, S.M., Lam, P.J., Ohnemus, D.C., Huang, K.F., Robinson, L.F., Lu, Y.B., Cheng, H., Edwards, R.L., Moran, S.B., 2015b. Intensity of Th and Pa scavenging partitioned by particle chemistry in the North Atlantic Ocean. Mar Chem 170, 49-60. doi:10.1016/j.marchem.2015.01.006.

Hayes, C.T., Anderson, R.F., Jaccard, S.L., Francois, R., Fleisher, M.Q., Soon, M., Gersonde, R., 2013. A new perspective on boundary scavenging in the North Pacific Ocean. Earth Planet Sc Lett 369, 86-97. doi:10.1016/j.epsl.2013.03.008.

Henderson, G.M., Anderson, R.F., 2003. The U-series toolbox for paleoceanography. Rev Mineral Geochem 52, 493-531. doi:10.2113/0520493.

Henry, L.G., McManus, J.F., Curry, W.B., Roberts, N.L., Piotrowski, A.M., Keigwin, L.D., 2016. North Atlantic ocean circulation and abrupt climate change during the last glaciation. Science 353, 470. doi:10.1126/science.aaf5529.

Hoffmann, S.S., McManus, J.F., Curry, W.B., Brown-Leger, L.S., 2013. Persistent export of 231 Pa from the deep central Arctic Ocean over the past 35,000 years. Nature 497, 603-606. doi:10.1038/nature12145.

Hoffmann, S.S., McManus, J.F., Swank, E., 2018. Evidence for Stable Holocene Basin-Scale Overturning Circulation Despite Variable Currents Along the Deep Western Boundary of the North Atlantic Ocean. Geophys Res Lett 45, 13,427-413,436. doi:10.1029/2018gl080187.

Jenkins, W.J., Smethie, W.M., Boyle, E.A., Cutter, G.A., 2015. Water mass analysis for the US GEOTRACES (GA03) North Atlantic sections. Deep-Sea Res Pt Ii 116, 6-20. doi:10.1016/j.dsr2.2014.11.018.

Johns, W.E., Baringer, M.O., Beal, L.M., Cunningham, S.A., Kanzow, T., Bryden, H.L., Hirschi, J.J.M., Marotzke, J., Meinen, C.S., Shaw, B., Curry, R., 2011. Continuous, Array-Based Estimates of Atlantic Ocean Heat Transport at 26.5 degrees N. J Climate 24, 2429-2449. doi:10.1175/2010JCLI3997.1.

Key, R.M., Kozyr, A., Sabine, C.L., Lee, K., Wanninkhof, R., Bullister, J.L., Feely, R.A., Millero, F.J., Mordy, C., Peng, T.H., 2004. A global ocean carbon climatology: Results from Global Data Analysis Project (GLODAP). Global Biogeochem Cy 18. doi:10.1029/2004gb002247.

Kumar, N., Gwiazda, R., Anderson, R.F., Froelich, P.N., 1993. Pa-231/Th-230 Ratios in Sediments as a Proxy for Past Changes in Southern-Ocean Productivity. Nature 362, 45-48. doi:10.1038/362045a0.

Lankhorst, M., Fratantoni, D., Ollitrault, M., Richardson, P., Send, U., Zenk, W., 2009. The mid-depth circulation of the northwestern tropical Atlantic observed by floats. Deep Sea Research Part I: Oceanographic Research Papers 56, 1615-1632. doi:10.1016/j.dsr.2009.06.002.

Lerner, P., Marchal, O., Lam, P.J., Anderson, R.F., Buesseler, K., Charette, M.A., Edwards, R.L., Hayes, C.T., Huang, K.-F., Lu, Y., Robinson, L.F., Solow, A., 2016. Testing models of thorium and particle cycling in the ocean using data from station GT11-22 of the U.S. GEOTRACES North Atlantic section. Deep Sea Research Part I: Oceanographic Research Papers 113, 57-79. doi:10.1016/j.dsr.2016.03.008.

Lerner, P., Marchal, O., Lam, P.J., Gardner, W., Richardson, M.J., Mishonov, A., 2020. A model study of the relative influences of scavenging and circulation on 230Th and 231Pa in the western North Atlantic. Deep Sea Research Part I: Oceanographic Research Papers 155, 103159. doi:10.1016/j.dsr.2019.103159.

Lippold, J., Gherardi, J.M., Luo, Y.M., 2011. Testing the Pa-231/Th-230 paleocirculation proxy: A data versus 2D model comparison. Geophys Res Lett 38, L20603. doi:10.1029/2011gl049282.

Lippold, J., Luo, Y.M., Francois, R., Allen, S.E., Gherardi, J., Pichat, S., Hickey, B., Schulz, H., 2012. Strength and geometry of the glacial Atlantic Meridional Overturning Circulation. Nat Geosci 5, 813-816. doi:10.1038/NGEO1608.

Lippold, J., Pöppelmeier, F., Süfke, F., Gutjahr, M., Goepfert, T.J., Blaser, P., Friedrich, O., Link, J.M., Wacker, L., Rheinberger, S., Jaccard, S.L., 2019. Constraining the Variability of the Atlantic Meridional Overturning Circulation During the Holocene. Geophys Res Lett 46, 11338-11346. doi:10.1029/2019gl084988.

Luo, Y., Francois, R., Allen, S.E., 2010. Sediment Pa-231/Th-230 as a recorder of the rate of the Atlantic meridional overturning circulation: insights from a 2-D model. Ocean Sci 6, 381-400. doi:10.5194/os-6-381-2010.

McManus, J.F., Francois, R., Gherardi, J.M., Keigwin, L.D., Brown-Leger, S., 2004. Collapse and rapid resumption of Atlantic meridional circulation linked to deglacial climate changes. Nature 428, 834-837. doi:10.1038/Nature02494.

Missiaen, L., Bouttes, N., Roche, D.M., Dutay, J.C., Quiquet, A., Waelbroeck, C., Pichat, S., Peterschmitt, J.Y., 2019. Carbon isotopes and Pa/Th response to forced circulation changes: a model perspective. Clim. Past Discuss. 2019, 1-26. doi:10.5194/cp-2019-45.

Missiaen, L., Menviel, L.C., Meissner, K.J., Roche, D.M., Dutay, J.-C., Bouttes, N., Lhardy, F., Quiquet, A., Pichat, S., Waelbroeck, C., 2020. Modelling the impact of biogenic particle flux intensity and composition on sedimentary Pa/Th. Quaternary Sci Rev 240, 106394. doi:10.1016/j.quascirev.2020.106394.

Moran, S.B., Shen, C.C., Edmonds, H.N., Weinstein, S.E., Smith, J.N., Edwards, R.L., 2002. Dissolved and particulate Pa-231 and Th-230 in the Atlantic Ocean: constraints on intermediate/deep water age, boundary scavenging, and Pa-231/Th-230 fractionation. Earth Planet Sc Lett 203, 999-1014. doi:10.1016/S0012-821x(02)00928-7.

NASA Goddard Space Flight Center, O.E.L., Ocean Biology Processing Group, 2018 Reprocessing. Moderate-resolution Imaging Spectroradiometer (MODIS) Aqua Chlorophyll Data, in: OB.DAAC, N. (Ed.), Greenbelt, MD, USA.

Ng, H.C., Robinson, L.F., McManus, J.F., Mohamed, K.J., Jacobel, A.W., Ivanovic, R.F., Gregoire, L.J., Chen, T., 2018. Coherent deglacial changes in western Atlantic Ocean circulation. Nature Communications 9, 2947. doi:10.1038/s41467-018-05312-3.

Nozaki, Y., Yang, H.-S., Yamada, M., 1987. Scavenging of thorium in the ocean. Journal of Geophysical Research: Oceans 92, 772-778. doi:10.1029/JC092iC01p00772.

Ohnemus, D.C., Lam, P.J., 2015. Cycling of lithogenic marine particles in the US GEOTRACES North Atlantic transect. Deep-Sea Res Pt Ii 116, 283-302. doi:10.1016/j.dsr2.2014.11.019.

Oudot, C., Morin, P., Baurand, F., Wafar, M., Le Corre, P., 1998. Northern and southern water masses in the equatorial Atlantic: distribution of nutrients on the WOCE A6 and A7 lines. Deep-Sea Res Pt I 45, 873-902. doi:10.1016/S0967-0637(98)00002-8.

Owens, S.A., Buesseler, K.O., Sims, K.W.W., 2011. Re-evaluating the U-238-salinity relationship in seawater: Implications for the U-238-Th-234 disequilibrium method. Mar Chem 127, 31-39. doi:10.1016/j.marchem.2011.07.005.

Pavia, F., Anderson, R., Vivancos, S., Fleisher, M., Lam, P., Lu, Y., Cheng, H., Zhang, P., Lawrence Edwards, R., 2018. Intense hydrothermal scavenging of 230Th and 231Pa in the deep Southeast Pacific. Mar Chem 201, 212-228. doi:10.1016/j.marchem.2017.08.003.

Pichat, S., Sims, K.W.W., François, R., McManus, J.F., Brown Leger, S., Albarède, F., 2004. Lower export production during glacial periods in the equatorial Pacific derived from (231Pa/230Th)xs,0 measurements in deep-sea sediments. Paleoceanography 19. doi:10.1029/2003PA000994.

Rempfer, J., Stocker, T.F., Joos, F., Lippold, J., Jaccard, S.L., 2017. New insights into cycling of 231Pa and 230Th in the Atlantic Ocean. Earth Planet Sc Lett 468, 27-37. doi:10.1016/j.epsl.2017.03.027.

Robinson, L.F., 2014. RRS James Cook Cruise JC094, October 13 – November 30 2013, Tenerife - Trinidad. TROPICS, Tracing Oceanic Processes using Corals and Sediments. Reconstructing abrupt Changes in Chemistry and Circulation of the Equatorial Atlantic Ocean: Implications for global Climate and deep-water Habitats.

Rowland, G.H., Ng, H.C., Robinson, L.F., McManus, J.F., Mohamed, K.J., McGee, D., 2017. Investigating the use of 232Th/230Th as a dust proxy using co-located seawater and sediment samples from the low-latitude North Atlantic. Geochim Cosmochim Ac 214, 143-156. doi:10.1016/j.gca.2017.07.033.

Schlitzer, R., 2012. Ocean Data View.

Siddall, M., Henderson, G.M., Edwards, N.R., Frank, M., Muller, S.A., Stocker, T.F., Joos, F., 2005. Pa-231/Th-210 fractionation by ocean transport, biogenic particle flux and particle type. Earth Planet Sc Lett 237, 135-155. doi:10.1016/j.epsl.2005.05.031.

Sigman, D.M., Hain, M.P., Haug, G.H., 2010. The polar ocean and glacial cycles in atmospheric CO2 concentration. Nature 466, 47-55. doi:10.1038/nature09149.

Thiagarajan, N., McManus, J.F., 2019. Productivity and sediment focusing in the Eastern Equatorial Pacific during the last 30,000 years. Deep Sea Research Part I: Oceanographic Research Papers 147, 100-110. doi:10.1016/j.dsr.2019.03.007.

Thomas, A.L., Henderson, G.M., Robinson, L.F., 2006. Interpretation of the Pa-231/Th-230 paleo circulation proxy: New water-column measurements from the southwest Indian Ocean. Earth Planet Sc Lett 241, 493-504. doi:10.1016/j.epsl.2005.11.031.

Vanicek, M., Siedler, G., 2002. Zonal fluxes in the deep water layers of the western South Atlantic Ocean. J Phys Oceanogr 32, 2205-2235. doi:10.1175/1520-0485(2002)032<2205:ZFITDW>2.0.CO;2.

Weatherall, P., Marks, K.M., Jakobsson, M., Schmitt, T., Tani, S., Arndt, J.E., Rovere, M., Chayes, D., Ferrini, V., Wigley, R., 2015. A new digital bathymetric model of the world's oceans. Earth and Space Science 2, 331-345. doi:10.1002/2015EA000107.

Wunsch, C., Ferrari, R., 2004. VERTICAL MIXING, ENERGY, AND THE GENERAL CIRCULATION OF THE OCEANS. Annual Review of Fluid Mechanics 36, 281-314. doi:10.1146/annurev.fluid.36.050802.122121.

Yang, H.S., Nozaki, Y., Sakai, H., Masuda, A., 1986. The Distribution of Th-230 and Pa-231 in the Deep-Sea Surface Sediments of the Pacific-Ocean. Geochim Cosmochim Ac 50, 81-89. doi:10.1016/0016-7037(86)90050-5.

Yu, E.F., Francois, R., Bacon, M.P., 1996. Similar rates of modern and last-glacial ocean thermohaline circulation inferred from radiochemical data. Nature 379, 689-694. doi:10.1038/379689a0.